

Universität Stuttgart

# **Microstructural Evolution in Spinodal Half-Heusler Thermoelectrics**

Diplomarbeit

**Jian Feng**

Institute of Materials Science  
University of Stuttgart  
Stuttgart, Germany

**2014**

By B.Sc. Jian Feng, born in Shanxi, China

Grade: 1.0

Examiner: Prof. Dr. A. Weidenkaff  
Prof. Dr. Dr. h.c. G. Schmitz  
Dr. H. Näfe

Institute of Materials Science  
University of Stuttgart  
Stuttgart, Germany

December 2014



# Abstract

Spinodal  $Zr_{0.4}Hf_{0.6}Ni_{1.15}Sn$  half-Heusler thermoelectrics are synthesized and aged. The complex microstructure due to the spinodal decomposition is investigated by powder X-ray diffraction (XRD), scanning electron microscope (SEM) and transmission electron microscope (TEM). By Rietveld refinements, it is confirmed that excess Ni atoms in the arc-melted and spark-plasma-sintered half-Heusler matrix prefer to form nanoscale/submicron Heusler precipitates via spinodal decomposition and growth during the aging at 1173 K. Such phase separation changes the band gap of semiconductors, reduces the thermal conductivity drastically and improves the performance of thermoelectrics. As a result, a more than 50 % improvement of the  $ZT$  value on the unaged specimens was achieved.

# Contents

<b>1. General introduction</b> .....	7
1.1 Focus .....	7
1.2 Crystal Structure .....	8
1.3 Band Structure .....	8
1.4 Thermoelectric half-Heusler Materials .....	10
1.5 Thermal Conductivity .....	11
1.6 Electronic Transport .....	15
1.7 Maximizing Figure of Merit .....	18
<b>2. Experimental</b> .....	21
2.1 Arc Melting .....	21
2.2 Vibratory disc mill .....	23
2.3 Spark Plasma Sintering .....	23
2.4 X-Ray Diffraction .....	26
2.5 Scanning Electron Microscopy .....	27
2.6 Determining Seebeck Coefficient and Electrical Conductivity .....	29
2.7 Determining thermal conductivity of bulk materials .....	30
2.8 Experimental uncertainty .....	31
2.9 Procedures .....	33
<b>3. Results and Discussions</b> .....	35
3.1 ICP-MS .....	35
3.2 XRD .....	35
3.3 Microstructure Analysis .....	37
3.3.1 AM Specimens .....	37
3.3.2 AS Specimens .....	41
3.3.3 Fracture Surface Analysis .....	46
3.3.4 Model for Microstructure Evolution .....	47
3.3.5 Thermoelectric Properties .....	48
<b>4. Conclusion</b> .....	52
<b>References</b> .....	53
<b>List of publications</b> .....	56
<b>Declaration of Authorship</b> .....	57

<b>Danksagung</b> .....	58
-------------------------	----

# 1. General introduction

## 1.1 Focus

Energy transformation or conversion is one of the most fundamental problems since the very beginning of mankind. Within the field of material science, thermoelectric materials have recently drawn much attention due to the increasing technological demands for energy conversion between heat and electricity.

The 18-electron half-Heusler (HH) alloys, which were discovered by Jeischoko [1] in 1970, have been proved to be promising thermoelectric materials in the past 15 years because of the high power factor and the thermal stability. However, the thermal conductivity of the compounds, such as  $MNiSn$ ,  $MCoSb$  ( $M=Ti, Zr, Hf$ ) and  $LnPbSb$ , is two or three times higher than those of conventional thermoelectric materials, which is disadvantageous to retain the heat at the junction and to reduce the heat transfer losses and furthermore to maximize the dimensionless figure of merit  $ZT$  [2].

Non-stoichiometric thermoelectrics especially excess Ni HH materials have been the focus of interest during the past few years, due to its fascinating microstructure and resulting enhancement of the thermoelectric performance. Hazama *et al.* [3, 4] studied the electronic structure and defect formation in  $TiNiSn$  system with excess Ni, using first-principles calculations and XPS data. They asserted that the excess Ni atoms randomly occupy the vacant sites in the HH structure, and act as phonon scattering centers resulting in significant improvement of the figure of merit without any substitution of expensive heavy elements such as Zr and Hf. Following this line of argument, Douglas *et al.* [5-7] obtained  $ZT$  value of 0.44 at 800 K with a composition  $TiNi_{1.15}Sn$  and pointed out that the excess Ni was not being statistically distributed, but rather occurred as coherent nanoclusters. According to these authors, the material system as a whole should be treated as an HH matrix with nanoclusters of Ni interstitial atoms pocketed throughout the material.

In the present work, non-stoichiometric HH alloys  $Zr_{0.4}Hf_{0.6}Ni_{1.15}Sn$  were synthesized aiming at systematically introducing defect states. The microstructure evolution due to Ni clusters in a buck HH thermoelectrics is focused. The elucidation of the interrelationships among aging time, precipitation tendency and thermoelectric properties especially Seebeck coefficient and thermal conductivity is investigated.

## 1.2 Crystal Structure

The  $MNiSn$  ( $M=Ti, Zr, Hf$ ) HH phases crystallize in a non-centrosymmetric cubic structure corresponding to the space group  $F\bar{4}3m$  (No. 216,  $C1_b$ , **Fig. 1a**). Within the lattice, the lighter and larger transition metal atoms ( $X$ ) occupy the Wyckoff position sites  $4a$   $[0, 0, 0]$  (white), the heavier and smaller transition metal atom ( $Y$ ) being at the position  $4c$   $[1/4, 1/4, 1/4]$  (light blue), while the metalloid ( $Z$ ) resides at the site  $4b$   $[1/2, 1/2, 1/2]$  (dark green). The crystal structure of the HH phase can be derived from the Heusler (H) structure (space group,  $Fm\bar{3}m$ , No. 225, **Fig. 1b**), formed from four interpenetrating  $fcc$  sublattices when one of two equivalent  $Y$ -sites is left empty.

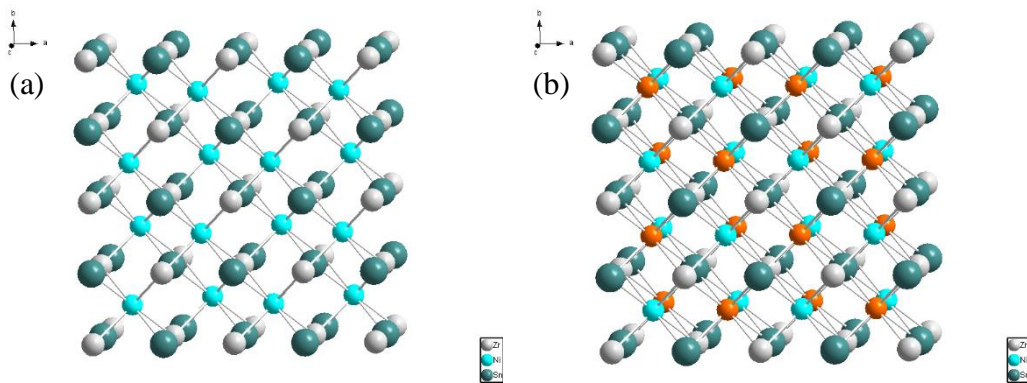


**Figure 1.** (a) Lattice of XYZ half-Heusler ( $X = Zr, Y = Ni, Z = Sn$ ) and (b) Heusler phases. Orange atoms represent Ni atoms sitting at the empty sublattice of half-Heusler phases.

## 1.3 Band Structure

Ögüt and Rabe [8] discussed not only the structural stability and electronic properties of the ternary intermetallic HH alloy  $MNiSn$  ( $M= Ti, Zr, Hf$ ) but also the closely related Heusler alloy  $MNi_2Sn$  on the basis of ab-initio pseudopotential total energy and band-structure calculations, which were performed with a plane-wave basis set using the conjugate gradients algorithm. These results described the lowest-energy phase of

*MNiSn* alloys as narrow-gap semiconductors with indirect gaps about 0.5 eV and a *SnM* rock salt structure sublattice, while the *MNi<sub>2</sub>Sn* as metallic. Both the *pd*-hybridization in the *SnZr* rocksalt substructure and the symmetry breaking due to the Ni sublattice were found to be crucial factors for the formation of the band gap.

Tobola and Pierre [9, 10] studied general aspects of the electronic structure of the XYZ HH systems classified according to the total number of valence electrons by using the Korringa–Kohn–Rostoker (KKR) computations within the local spin density approximation (LDA) framework. They asserted that numerous HH systems with 18 valence electrons should exhibit semiconducting properties, unless a significant disorder, occurring mainly in the X and Y sublattices, may turn a system to a semi-metallic state. They emphasized that the hybridization/covalency between elements is very strong in HH alloys. The wave functions below the gap at or close to the Fermi level (mostly Ni, Co, Fe, Mn *d*-states) are expected to have a bonding character with the states of the other transition metal, which ensures the cohesion and the hard and brittle character of the alloys. By contrast, wave functions above the gap (mostly Ti, V states) are expected to have an anti-bonding nature. This conclusion might be significant for our later band engineering work.

The width of the band gap in HH alloys can be tuned from zero to 4 eV [11]. The band gap in HH with 18 valence electron content (VEC) can be adjusted from zero to 1.1 eV [12] by tuning the chemical composition, whereas a larger difference in the electronegativity (EN) between the elements leads to larger band gaps [8]. Therefore, the calculated energy gap of TiNiSn (0.45 eV) [9, 13] is smaller than ZrNiSn (0.50 eV) [8], due to the larger difference in EN of Zr (1.3) compared to Ti (1.54). However, the experimental data of the band gap of HH alloys usually reveals much lower values, e.g. for TiNiSn (0.12 eV) and ZrNiSn (0.19 eV) [8, 14]. This discrepancy between experimental and calculated values is due to antisite disorder within the HH structure.

### 1.4 Thermoelectric half-Heusler Materials

HH alloys are admitted to be promising thermoelectrics and widely studied. The majority of the high-performance HH thermoelectrics are based on two systems: ZrNiSn for the *n*-type with a band gap of 0.55eV [9] and TiCoSb for the *p*-type materials with a band gap of 0.95eV [9]. Within a single HH thermoelectrics, as shown in **Fig. 2**, merely via doping on one or two sites of the three occupied *fcc* sublattices, small thermal conductivity ( $\kappa < 4$  W/Km) and significantly high power factors and *ZT*s are obtained. Concretely, site substitution with isoelectronic elements used to reduce the thermal conductivity due to mass and strain fluctuations, while site substitution with non-isoelectronic elements via electronic doping, significantly affects carrier concentration i.e. the transport properties in HH thermoelectrics. Donors introduce additional electrons into the HH system and lead to a shift of the Fermi energy towards higher energy and thus increase the band gap. The minority carriers are suppressed and the Seebeck coefficient shifts to higher temperatures. On the contrast, acceptors introduce holes into the system and shift the Fermi energy towards the valence band [2].

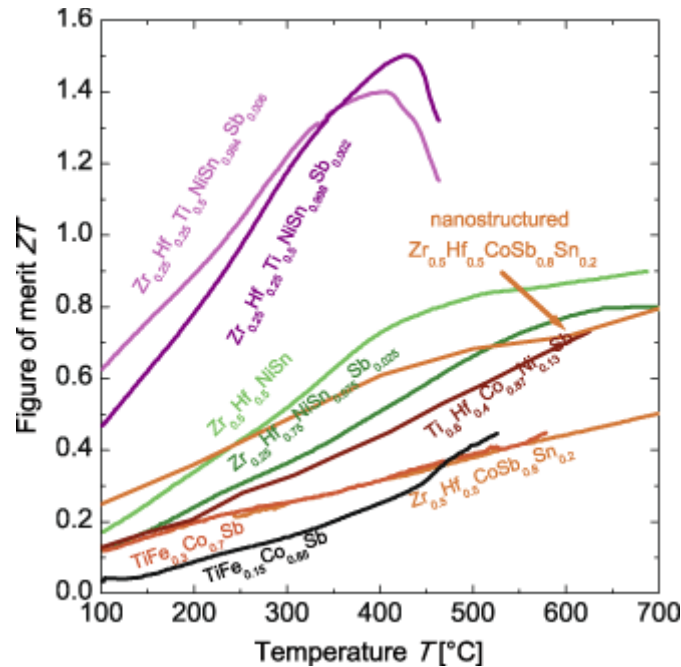


**Figure 2.** The state-of-the-art thermoelectric figure of merit *ZT* of half-Heusler materials. [15]

Electronic doping of small amounts of transition metals into the HH system introduces local variation in the density of states (DOS) near or within the band gap region (resonate levels). **Fig. 3** demonstrates the dopant-induced change in the chemical potential, leading to peaks in the Seebeck coefficient near the Fermi level. It should be noticed that small doping states lead to a considerable shift of the Fermi level and therefore improve the electronic properties. Besides doping, antisite disorder and point defects, nanostructuring, microstructure tuning and band structure engineering are also effective methods to enhance the thermoelectric properties of the HH materials.

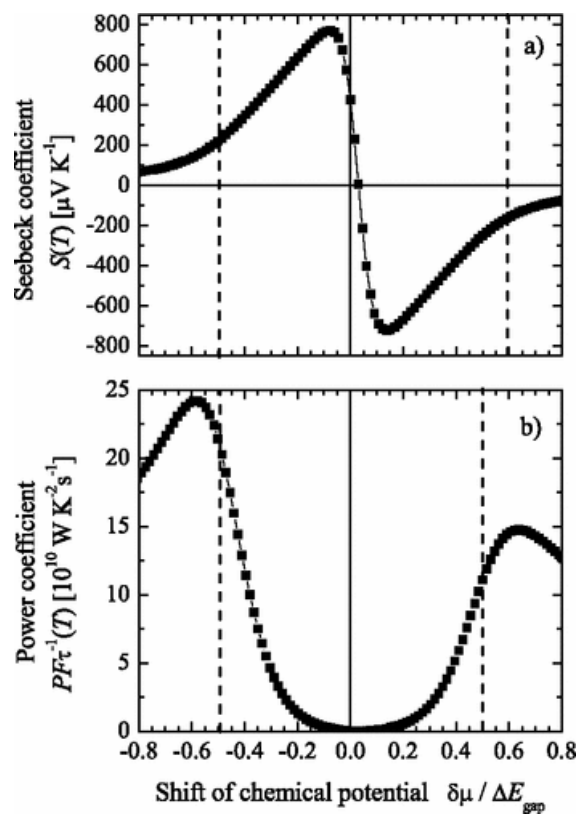


**Figure 3.** Calculated Seebeck and power coefficients of TiNiSn. The shift of the chemical potential is given with respect to the size of the gap. The valence and conduction band extrema are marked by dashed lines ( $T = 300\text{K}$ ) [16].

### 1.5 Thermal Conductivity

Thermal conductivity is the property of a material to conduct heat. Heat energy can be transmitted through solids via electrical carriers, lattice waves, electromagnetic waves, spin waves, or other excitations. In metals, electrical carriers i.e. the moving free electrons carry the majority of the heat, while in insulators, which do not possess free

electrons, lattice waves i.e. the vibration of the atoms are the dominant heat transporter. Generally, the total thermal conductivity  $\kappa$  can be written as a sum of all excitations:

$$\kappa = \sum_{\alpha} \kappa_{\alpha} \quad (1)$$

where  $\alpha$  denotes an excitation. Due to the differences in specimen size for single crystals or grain size for polycrystalline specimens, lattice defects or imperfections, dislocations, grain boundaries, interfaces, inclusions, precipitations, carrier concentrations, interactions between the carriers and the lattice waves, interactions between magnetic ions and the lattice waves, etc., induce the thermal conductivity of solids to vary drastically from one material to another.

Just like most of the non-equilibrium transport parameters, thermal conductivity cannot be predicted exactly. Actually, the most calculations and computer simulations of thermal conductivity are based on the Boltzmann transport equation (BTE), which was devised by Ludwig Boltzmann in 1872 and is considered to be the basis for analyzing the microscopic processes of heat conduction. BTE is a linear stochastic partial differential equation and the details of solving the equation are included in the literature [17, 18].

Simply, the kinetic formulation of thermal conduction can be expressed as:

$$\kappa = -\frac{1}{3} \sum_{\alpha} C_{\alpha} \tau_{\alpha} l_{\alpha} \quad (2)$$

where  $C_{\alpha}$  is the total heat capacity,  $\tau_{\alpha}$  is the average interval between collisions of two particles or relaxation time and  $l_{\alpha}$  the particle mean free path. This equation can be rewritten in terms of the measurable temperature dependent quantities

$$\kappa = C_p(T) \cdot \rho(T) \cdot D(T) \quad (3)$$

where  $D(T)$  is the thermal diffusivity, which is the quantity that provides information about the time required until an effect of the applied change in temperature can be recognised,  $C_p(T)$  specific heat capacity and  $\rho(T)$  density.

For the case of thermoelectrics, thermal conductivity can be divided into two major components

$$\kappa = \kappa_{\text{ph}} + \kappa_{\text{el}} \quad (4)$$

The lattice component to the thermal conductivity  $\kappa$  is due to the heat transported by phonons ( $\kappa_{\text{ph}}$ ) and is low for amorphous or disordered materials. The electronic component to the thermal conductivity,  $\kappa_{\text{el}}$ , is due to the heat transported by the electrons and can be estimated from the Wiedemann–Franz law, which relates  $\kappa$  to the electrical resistivity  $\rho$ .

$$\kappa_{\text{el}} = L(T, n) \cdot \sigma(T) \cdot T = L(T, n) \cdot n(T) \cdot e \cdot \mu(T) \cdot T \quad (5)$$

where  $L(T, n)$  is the Lorentz number,  $2.4 \times 10^{-8} \text{ W}\Omega\text{K}^{-2}$  for free electrons. Muta *et al.* [19] obtained a Lorentz number of  $1.6 \times 10^{-8} \text{ W}\Omega\text{K}^{-2}$  in Nb-doped  $M\text{NiSn}$  ( $M = \text{Ti, Zr}$ ) HH compounds. Value for  $L(T, n)$  of  $\text{Hf}_{0.65}\text{Zr}_{0.35}\text{Ni}_{1-x}\text{Pt}_x\text{Sn}_{0.98}\text{Sb}_{0.02}$  published by Xie *et al.* [20] are illustrated in **Fig. 4**, calculated according to the expression

$$L = -\frac{k_{\text{B}}^2 (1 + \lambda)(3 + \lambda)F_{\lambda}(\eta)F_{2+\lambda}(\eta) - (2 + \lambda)^2 F_{1+\lambda}(\eta)^2}{e^2 (1 + \lambda)^2 F_{\lambda}(\lambda)^2} \quad (6)$$

where  $\lambda$  is the scattering factor and  $\eta$  the reduced chemical potential.

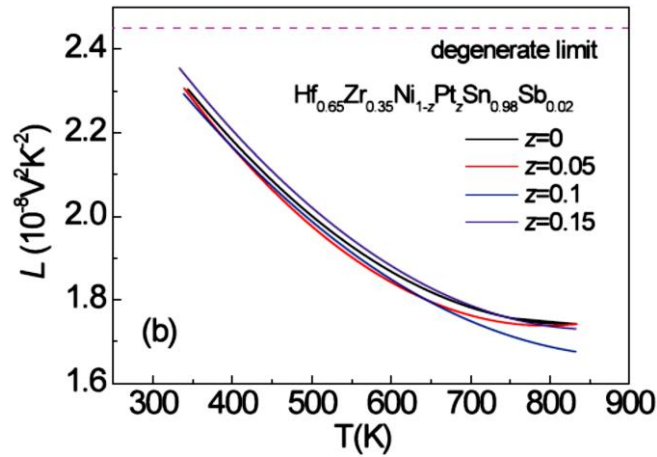


**Figure 4.** Temperature dependence of the Lorenz number for  $Hf_{0.65}Zr_{0.35}Ni_{1-x}Pt_xSn_{0.98}Sb_{0.02}$  [20].

Besides, the quantum mechanical description of the electrical conductivity, in which electrons are in a band that is strictly parabolic, is demonstrated below:

$$\sigma = \frac{ne^2\tau}{m^*} \quad (7)$$

where  $n$  is the number of electrons per unit volume,  $\tau$  relaxation time,  $m^*$  effective mass and  $e$  electron charge. From Equations (2) and (7) it can be noticed that the very central problem in transport theory is the calculation of the relaxation time  $\tau$ . An empirical rule described by Matthiessen in 1862 [21] declares that if several distinct scattering mechanisms are at play, the overall resistivity is simply the sum of the resistivity one would obtain if the individual scattering mechanism alone was present. The essentials behind Matthiessen's Rule is the independence of scattering mechanisms; that is, the overall collision rate is the sum of the collision rates of the participating individual scattering processes. In the context of the relaxation time approximation this immediately leads to a reciprocal addition of the relaxation times:

$$\tau^{-1} = \tau_N^{-1} + \tau_U^{-1} + \tau_{TD}^{-1} + \tau_B^{-1} + \tau_{EP}^{-1} \quad (8)$$

Thermal conductivity is representatively limited by phonon-phonon scattering, phonon-electron scattering (EP), point defect scattering and boundary scattering. Normal (N) and Umklapp (U) scattering are phonon-phonon interactions. The normal process

conserves the total phonon momentum, while the Umklapp process changes phonon momentum. The Umklapp process is often the dominant mechanism at temperatures above Debye temperature and generates a conspicuous reduction of the thermal conductivity [22]. Point defect scattering (PD) arises from mass and strain fluctuation. For multicomponent materials or nanostructured alloys, the boundary scattering (B) reduces  $\kappa$  dramatically. Furthermore, Umklapp and point defect scattering target on high frequency phonons, while boundary scattering is often the dominant scattering mechanism at low frequencies (**Fig. 5**), which carry the largest portion of heat [23, 24]. As to the temperature dependence of  $\kappa$ , at low temperature, the boundary and defect scattering dominates and  $\kappa \propto T^{-3}$ , while at high temperature, Umklapp process prevails and  $\kappa \propto T^{-1}$  [17, 18, 25].

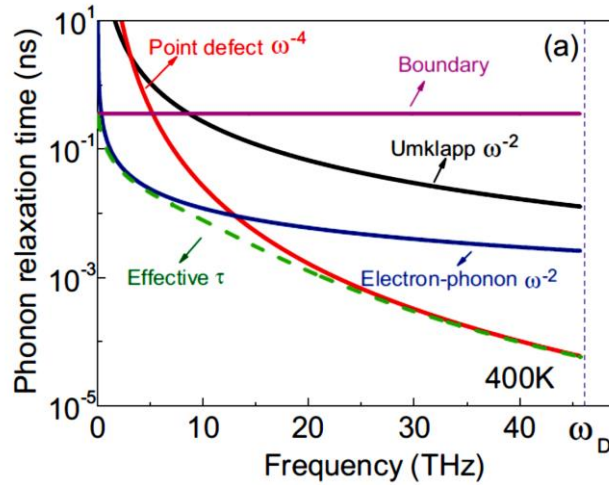


**Figure 5.** The frequency dependence of phonon relaxation time at 400 K for  $Hf_{0.65}Zr_{0.35}Ni_{0.85}Pt_{0.15}Sn_{0.98}Sb_{0.02}$  [20].

## 1.6 Electronic Transport

The very spirit of band engineering is the tuning of the Fermi level and the density of states. BTE provides a general understanding of the thermopower which is expressed by the Mott-equation [26]

$$S = \frac{\pi^2}{3} \frac{kT^2}{q} k_B T \left\{ \frac{d[(\sigma(E))]}{dE} \right\}_{E=E_F}$$

$$= \frac{\pi^2 kT^2}{3 q} k_B T \left\{ \frac{1}{n} \frac{dn(E)}{dE} + \frac{1}{\mu} \frac{d\mu(E)}{dE} \right\}_{E=E_F} \quad (9)$$

with  $\sigma(E) = 1/\rho(E) = n(E)e\mu(E)$  [27].  $\sigma(E)$  is the electronic conductivity determined as a function of the band filling or Fermi energy  $E_F$ . If electronic scattering is independent of energy, then  $\sigma(E)$  is proportional to the DOS at  $E$ .  $\mu(E)$  is the mobility,  $q$  the carrier charge and  $d[(\sigma(E))]/dE$  is the slope of the DOS. The following image explains the significance of the Mott-equation.

It should be noticed that the Mott-equation demonstrates a conflict between the Seebeck coefficient  $S$  and the carrier concentration. How to maintain a high  $S$  without degrading  $\sigma$  remains a challenge for the materials researchers [28, 29].

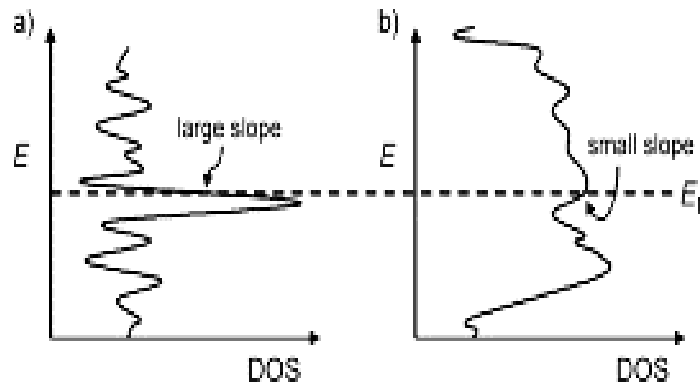


**Figure 6.** Hypothetical density of state (DOS) with (a) a large slope  $d[(\sigma(E))]/dE$  and (b) a small slope near  $E_F$  [30].

For degenerate semiconductors [12, 28], the Mott equation can also be expressed in terms of DOS effective mass  $m^*$  [23] according to the Mahan-Sofo theory [31]

$$S = \frac{8\pi^2 k_B^2 T}{3qh^2} m_d^* \left( \frac{\pi}{3n} \right)^{\frac{2}{3}} \quad (10)$$

with  $n(E) = g(E)f(E)$  and

$$g(E) = \frac{(m_d^*)^{\frac{3}{2}}}{\hbar^3 \pi^2} \sqrt{2E} \quad (11)$$

where  $n(E)$  is the carrier density at the energy level  $E$ ,  $f(E)$  is the Fermi function,  $q$  the carrier charge,  $\mu(E)$  the mobility,  $g(E)$  the local increase in the density of states (DOS) over a narrow energy range  $E_R$ , as illustrated in **Fig. 7**. Equation (10) and (11) actually offer the muse of the enchantment of the thermoelectric properties via introduction of resonant states into thermoelectric material systems (**Fig. 7b**). At the meantime, the increase in effective mass can also be used to characterize the resonant states phenomenon.

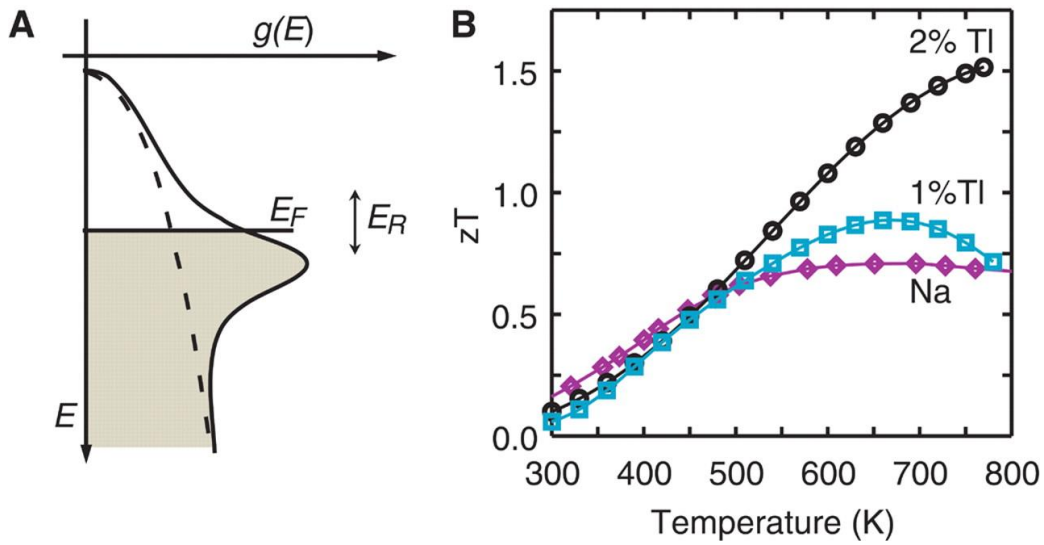


**Figure 7:** (a) The figure of merit  $ZT$  is optimized when the Fermi energy  $E_F$  falls in the distortion energy range  $E_R$ . (b) The  $ZT$  values for resonant levels enhanced  $Tl_{0.02}Pb_{0.98}Te$  (black squares) and  $Tl_{0.01}Pb_{0.99}Te$  (blue circles) compared to that of a reference specimen of  $Na-PbTe$  (purple diamonds) [32].

The DOS effective mass  $m_d^*$  increases with flat narrow bands i.e. small curvature of the band, which leads to a high DOS at the Fermi level. The relationship between the effective mass of the charge carriers and the mobility is:

$$\mu(E) = q \frac{\tau(E)}{m^*} \quad (12)$$

with  $\tau(E) = \tau_0 E^\Lambda$ , where  $\tau(E)$  is the relaxation time and  $\Lambda$  the scattering exponent, measured via Nernst coefficient measurements. Heavy carriers will move with slower velocities and therefore smaller mobility. Thus it is also required to pursue a balance between the effective mass of the dominant charge carriers and high mobility.

### 1.7 Maximizing Figure of Merit

When a temperature gradient  $\Delta T$  is applied to a material, the mobile charge carriers, e.g. electrons, at the hot end tend to diffuse to the cold end. The build-up of charge carriers results in a net charge (negative for electrons,  $e^-$ , positive for holes,  $h^+$ ) at the cold end, producing an electrostatic field. An equilibrium is thus reached between the chemical potential for diffusion or charge flow and the electrostatic repulsion due to the build-up of charge. This merit, known as the Seebeck effect, is the very basis of thermoelectric power generation. TE devices (**Fig. 8**) contain many TE couples (**Fig. 8 bottom**) wired electrically in series and thermally in parallel (**Fig. 8 top**). The  $\Delta T$  causes the voltage while the heat flow drives the electrical current, which determines the power output. The efficiency of a TE material for power generation can be described as below:

$$\eta_{TE} = \eta_C \left( \frac{(1 + zT_M)^{\frac{1}{2}} - 1}{(1 + zT_M)^{\frac{1}{2}} + \frac{T_C}{T_H}} \right) \quad (13)$$

where  $\eta_C$  is the Carnot efficiency with  $\eta_C = \frac{T_H - T_C}{T_H}$ ,  $T_H$  is the hot-side temperature,  $T_C$  is the cold-side temperature, and  $T_M$  is the average temperature. The maximum efficiency of a TE device is determined by its figure of merit ( $ZT$ ), which is defined as:

$$zT = \frac{S^2 \sigma T}{\kappa} \quad (14)$$

and the term  $S^2 \sigma$  is designated as powerfactor.

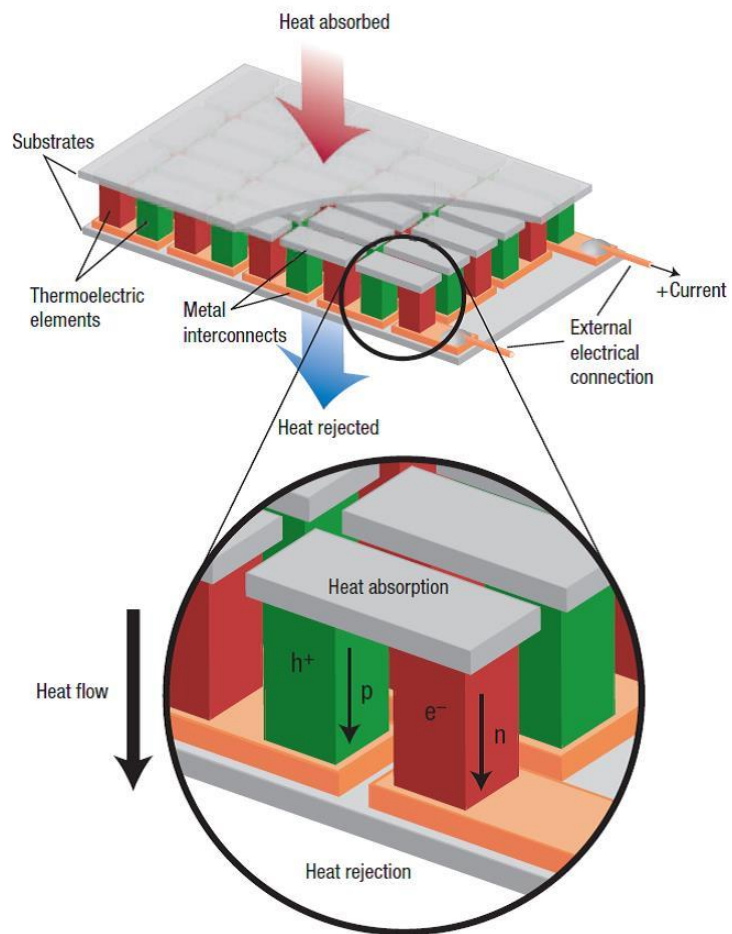


**Figure 8.** Thermoelectric devices [32].

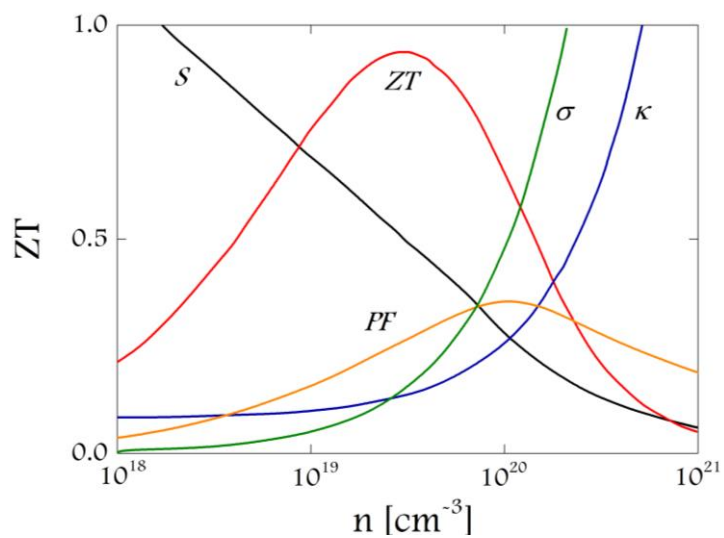


**Figure 9.** Maximizing  $ZT$  through carrier concentration tuning [32].

The basic idea to maximize the  $ZT$  value is demonstrated in **Fig. 9**. It shows the compromise between large Seebeck coefficient  $S$  and high electrical conductivity  $\sigma$  in thermoelectric materials that must be struck to maximize the figure of merit  $ZT$ . This peak typically occurs at carrier concentrations of  $10^{19} \sim 10^{21} \text{ cm}^{-3}$ , depending on the material system, which falls in between common metals and heavily doped semiconductors. General strategies towards a higher  $ZT$  value can be accomplished by band engineering due to the raise of the carrier concentration or by decreasing the thermal conductivity due to an effective phonon scattering by defects and microstructure tuning

## 2. Experimental

### 2.1 Arc Melting

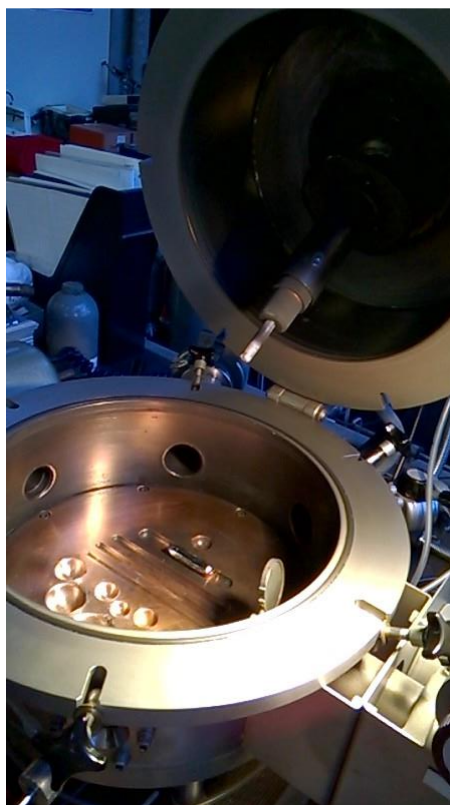


*Figure 10. AM furnace device with water-cooled copper hearth plate mold, located in Max-Planck-Institute Stuttgart.*

The method used in this work to synthesize the  $\text{Hf}_{0.6}\text{Zr}_{0.4}\text{Ni}_{1.15}\text{Sn}$  series of alloys is arc melting (AM), a simple but effective method. HH alloys contain elements like Hf, Zr, and Ti which, when heated, react with oxygen to form oxides. Oxides are detrimental to premium quality melted thermoelectrics. HH alloys can be protected from the atmosphere and residuals by melting inside a container protected by argon gas. This approach provides more control over alloy chemistry. The result is a clean, more uniform product with superior properties required for critical service applications. The AM process effectively removes dissolved gas and inclusions, so that AM is also the final melting step for many aerospace alloys, especially high-temperature titanium alloys used for rotating parts [33].

In the AM furnace (**Fig. 10**), DC electric current is passed through the electrode. The electric arc that is created is similar to a welding arc and produces the necessary heat for melting and re-melting of the electrode. Metal droplets form on the bottom of the electrode, thereby melting the electrode inside the vacuum chamber. The melted materials solidify very quickly inside a water-cooled copper hearth plate mold (**Fig. 10**). This process will eliminate ingot macro-segregation and significantly reduces micro-segregation. The subsequent heat treatment and hot working of the ingot will eliminate the remaining chemical segregation of the microstructure. On the other hand, for the fragile alloys or HH alloys in our case, the high cooling rate tends to complicate the further mechanical deformation, because of the existence of micro-cracks (**Fig. 11**), owing to the great temperature gradient between the top and bottom of the specimen.



**Figure 11.** A broken specimen owing to microcracks.

The synthesis process of a specimen includes a number times of melting (4 times in this work), with the specimen being turned over each time in order to ensure a good homogeneity of the elements in the alloy. The specimen is weighed after each melting to control possible weight losses, which must be negligible, smaller than 0.5 at. % in this work, to maintain the desired stoichiometry. An alternative method to laboratory synthesis HH alloy is the electric induction furnace, which is a type of melting furnace that uses electric currents to melt metal. Induction furnaces are ideal for melting and alloying a wide variety of metals with minimum melt losses, however, refining in induction furnace is not as intensive or effective as in an AM furnace. In industry, the use of AM allows steel or titanium to be made from a 100 % scrap metal feedstock. This

greatly reduces the energy required to produce metals when compared with primary metal-making from ores. Another benefit of AM is flexibility, AM can be rapidly started and stopped, allowing the furnace to vary production according to demand.

## **2.2 Vibratory disc mill**

A vibratory disc mill under an argon atmosphere is suitable for an extremely quick, loss-free and reproducible grinding of medium-hard, brittle and fibrous materials to analytical fineness. The function principle is rather simple: the instrument comminutes by impact and friction. The instrument runs steadily, even with heavy grinding set and at high speed. The material of grinding rings is hardened steel. The grinding set is firmly attached to the vibration plate with a quick-action lever. The plate with the grinding set is subjected to circular horizontal vibrations. The centrifugal force acting on the grinding rings in the dish results in extreme pressure, impact and frictional forces acting on the specimen, producing fine particles in 15 seconds in this work. The circular vibrations are produced by a frequency controlled 1.5 kW motor. The vibratory disc mill achieves grind sizes below 100 microns within seconds and with excellent reproducibility. In this work, it is used for the preparation of the XRD powder specimens.

## **2.3 Spark Plasma Sintering**

Spark Plasma Sintering (SPS) is a high-speed powder consolidation and sintering technology capable of processing conductive and nonconductive materials. The mechanism is based on the electrical spark discharge phenomenon wherein a high-energy, low-voltage pulse current momentarily generates spark plasma at high temperatures in delicate local areas between particles. Generally, the operational temperatures are from 200 to 2400°C. Considering the pressure and temperature rise plus hold time, the whole process is completed in approximately 10 to 35 minutes. The relatively low temperatures together with fast processing times ensure control over grain growth and microstructure. SPS exploits uniaxial force and DC pulse energizing (Fig. 12a).

In SPS process, pressure plays an important and predictable role in curbing particulate growth and influencing overall densities. Pressure multiplies spark initiation

throughout the specimen as the material moves under pressure, especially during critical out-gassing stages. Both too much and too little pressure can negatively influence the densification. With too little pressure, the driving force for sintering is too small, according to Gibbs-Thomson's relations. With too much pressure, the grain boundaries move too fast and the vacancies cannot attach on the grain boundaries and be embedded in the interior of the grains (left behind). In large specimens where high density is required, force is commonly increased in stages to enhance out-gassing and electrical diffusion.

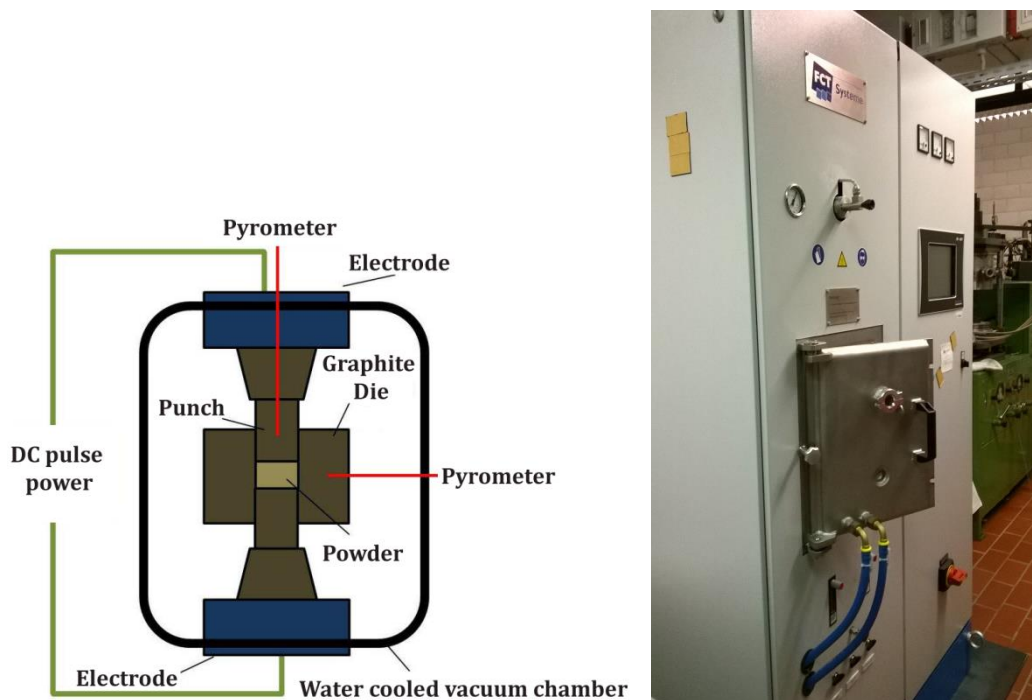


**Figure 12.** (a) Schematic diagram of SPS device (b) an SPS device located in Max-Planck-Institute Stuttgart.

SPS is especially high effective for nanocrystalline structures. Generally, fine materials have much more surface area per volume than the same material made of larger particles, nevertheless, in theory, the particles interact is also compacted, i.e. the interaction would be amplified, and the resulting material characteristics just like strength, wear resistance, magnetism and most importantly thermoelectricity would be boosted. Suitable applications include advanced lightweight armament, guidance optics, and ultra-high-strength tooling. Since SPS technology can sinter nanocrystalline materials with very little grain growth and negative particulate effect, many common materials may well find new applications with substantially improved characteristics.

Another advantage of SPS technology is that it can sinter materials without the use of binders. Most conventional powdered material sintering technologies require pre-forming and binders, and in many cases, expensive binder removal processes. Nevertheless, binders would weaken the workpiece due to their susceptibility to chemical wear, reduced hardness and strength, and oxidation breakdown.

During conventional sintering, many workpiece failures occur due to internal stress and microcracks caused by heat migration. SPS technology binds particles with electrical discharge energy throughout the workpiece. The heat is simultaneously consistent on the outside of the part and the center. Together with the relatively high speed of the process, this eliminates much of the internal stress commonly seen in conventionally sintered parts. High temperature, high pressure along with short aging time is beneficial for the existence of dislocations. Unfortunately, the quantitative study of the dislocation density is inadequate.

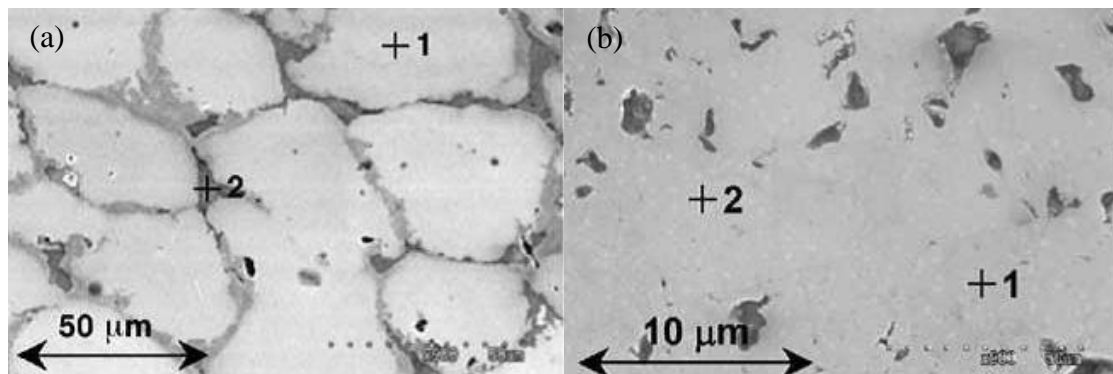


**Figure 13.** The microstructure of the arc-melted specimen. (a) The grain matrix composed of HH alloy is represented by +1, and the grain boundary composed of Ti–Sn based alloy is represented by +2. (b) The microstructure of the SPS specimen: The SPS temperature is 1173 K. The Ti-rich and Ti-poor HH phases are represented by +1 and +2, respectively [34].

SPS technology is capable of achieving nearly 100% theoretical density (99.6% in our case, calculated from density) in almost any metallurgical or ceramic material, it should be noticed that such a high theoretical density can only be achieved when some grain growth is considered. Furthermore, SPS process expenses are regularly 50 to 80% less than conventional sintering technologies, primarily due to the speed of the process. Most SPS applications only require minutes in comparison to the hours needed with conventional sintering systems.

Obviously, the SPS temperature impacts the thermoelectric properties of materials. Kurosaki *et al.* [34] studied the effect of SPS temperature on the thermoelectric properties of titanium based half-Heusler alloys  $(\text{Zr}_{0.6}\text{Hf}_{0.4})_{0.7}\text{Ti}_{0.3}\text{NiSn}$ , with AM specimen as a reference. The microstructure of the AM+SPS and AM specimens are shown below (**Fig. 13**). The refinement of the structure is evident. The grain boundaries rich of binary intermetallic compounds are disappeared and replaced by the Ti-rich and Ti-poor phases contrast. This report demonstrated that it can be achieved that the thermal conductivity is efficiently reduced without degradation of the electrical performance by the SPS process. As illustrated in **Fig. 14**, the *ZT* of SPS specimen at 1173 K reaches 0.43 at 760 K, which is 30% higher than that of the arc-melted specimens. The temperature 1173 K is then treated as conventionalized SPS temperature for *MNiSn* ( $M=\text{Ti, Zr, Hf}$ ) HH systems.

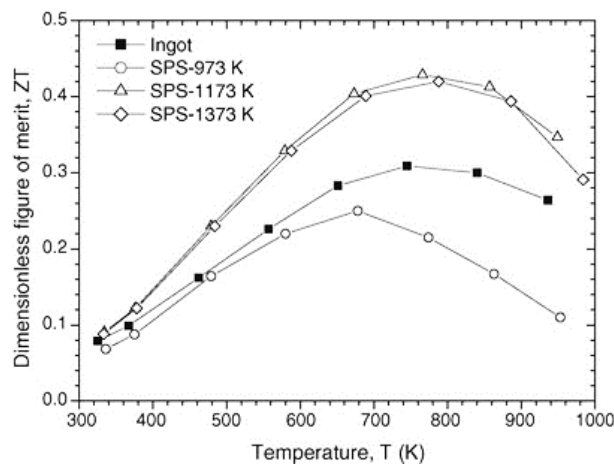


**Figure 14.** Temperature dependence of the *ZT* of arc-melted and spark plasma sintered specimens [34].

## 2.4 X-Ray Diffraction

X-ray diffraction (XRD) is used for identification of compounds and phases. Any crystalline material will produce a diffraction pattern that is characteristic of its constituents. Identification is aided by search and match software which compares experimental data with standard patterns from Inorganic Crystal Structure Database (ICSD) or the International Centre for Diffraction Data (ICDD) reference database. The preferred orientation of the crystallites within a polycrystalline material can have a profound effect on its physical and mechanical properties. By monitoring the variation of

intensity of the diffracted X-ray from a specific set of lattice planes, it is possible to determine both the direction and the magnitude of this preferred orientation implying texture analysis.

Residual stress, as well as dislocations in a specimen, will cause very small changes to its inter-planar spacing. The magnitude of these changes will depend on the degree of stress and the orientation of the crystallites with respect to the stress. By determining the inter-planar spacing for crystallites of different orientations it is possible to calculate the residual stress as well as dislocation densities from the measured strain in the lattice. For that purpose, there is no need to measure the specimen in an unstressed state. Besides, XRD provides information about crystal structures and lattice parameters; also it allows calculation of vacancy concentration and measurement of the degree of crystallinity and crystallite size. XRD measurements can be performed at elevated temperatures even up to 1000 °C, which enables the thermal behavior of lattice parameters to be characterized, and investigations of crystallization and high-temperature phases and phase transformations. The high-temperature chamber is fitted with a system to allow measurements to be made in controlled atmospheres so that structural changes related to specimen-gas interactions can be studied.

## 2.5 Scanning Electron Microscopy

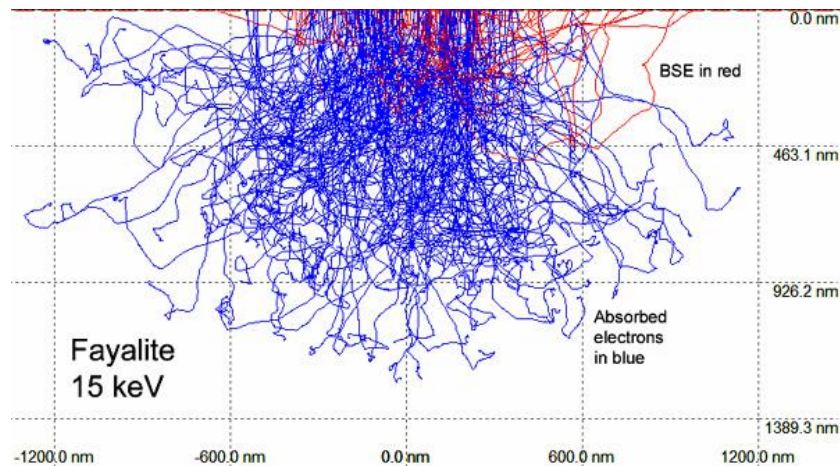


**Figure 15.** Simulation of 15 keV electrons in fayalite ( $\text{Fe}_2\text{SiO}_4$ ). Paths of backscattered electrons are in red, while those of absorbed electrons in blue. This slice is taken through

a three-dimensional volume. Copyright of the image belongs to Northern Arizona University.

Scanning electron microscopy (SEM) is the usual method for high-resolution imaging of surfaces. The SEM uses electrons for imaging, just like a light microscope uses visible light. The advantages of SEM over light microscopy include much higher magnification ( $>100,000\times$ ) and greater depth of field of up to 70 times that of light microscopy (max.  $1,600\times$ ). Qualitative and quantitative chemical analysis information is also obtained using an energy dispersive x-ray spectrometer (EDX) with the SEM.

In an electron column above the specimen chamber, SEM generates a beam of incident electrons that are produced by a thermal emission source, such as a heated tungsten filament, or by a field emission cathode. The energy of the incident electrons can be as low as 100 eV or as high as 30 keV depending on the evaluation objectives. By a series of electromagnetic lenses in the SEM column, the electrons are focused into a small beam, which is scanned in a raster pattern over the surface for imaging. The beam can also be focused as small as about 1 nm at a single point or scanned along a line for x-ray analysis.

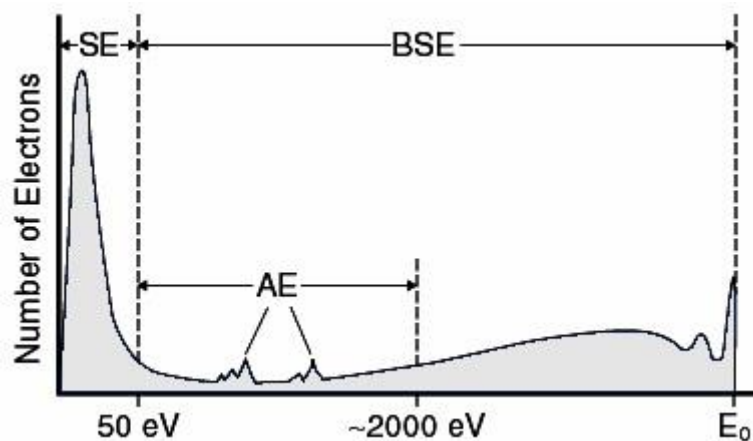


**Figure 16:** SE forms a large low-energy peak. Auger electrons (AE) produce relatively small peaks on the BSE distribution.

The incident electrons cause electrons to be emitted from the specimen due to elastic and inelastic scattering processes within the specimen's surface and near-surface region. The volume of electron interaction may be modeled from first principles using a Monte Carlo method, where the paths of a series of incident electrons are restricted probabilistically with equations for elastic and inelastic scattering determining the

scattering angles, mean-free-paths, and the rate of energy loss (**Fig. 15**). High-energy electrons that are bounced by an elastic collision of an incident electron, typically with a specimen atom's nucleus, are referred to as backscattered electrons (BSE). The energy of backscattered electrons will be comparable to that of the incident electrons. Emitted lower-energy electrons resulting from inelastic scattering are called secondary electrons (SE). SE can be formed by collisions with the nucleus where substantial energy loss occurs or by the rebound of loosely bound electrons from the specimen atoms. As shown in Fig. 16, the energy of secondary electrons is typically 50 eV or less in the electron energy spectrum.

Predominantly, two electron detector types are used for SEM imaging. Scintillator type detectors are used for SE imaging. This detector is charged with a positive voltage to attract electrons to the detector for improved signal-to-noise ratio. Detectors for BSE can be scintillator types or a solid-state detector. The quality and resolution of SEM images are a function of three major parameters: instrument performance, selection of imaging parameters or the operator, and nature or the preparation of the specimen. All three aspects operate concurrently and neither of them should or can be ignored or overemphasized. SEM is operated under high vacuum, so the specimens must be compatible with high vacuum ( $10^{-7} \sim 10^{-5}$  mbar). Therefore, liquids and materials containing liquids and other volatile components cannot be studied directly. Also, fine powder specimens can be examined with the proper substrate. Non-conductive materials should be coated with a thin conductive film by sputtering or evaporation then attached to a conductive specimen holder. Typical coating materials can be Au, Pt, Pd and also their alloys, as well as carbon, without significantly affecting observed surface morphology.

## **2.6 Determining Seebeck Coefficient and Electrical Conductivity**

ZEM-3 (ULVAC) is used to measure Seebeck coefficient and electrical resistance. A prism (10 x 2 x 2 mm) specimen is set in a vertical position between the upper and lower blocks in the heating furnace. While the specimen is continuously heated and held at specified temperature points from room temperature to 1200 °C, it is heated

by the heater in the lower block to provide a temperature gradient. The relative Seebeck coefficient  $\Delta S$  is measured by measuring the upper and lower temperatures  $T_1$  and  $T_2$  with the thermocouples pressed against the side of the specimen, followed by measurement of thermal electromotive force  $dV$  between the same wires on one side of the thermocouple:

$$\Delta S = \lim_{dT \rightarrow 0} \frac{dV}{dT} \quad (15)$$

where  $dT = T_2 - T_1$ . In this research,  $S$  of HH alloys is measured with respect to copper (e.g. +2.7  $\mu\text{V/K}$  at RT). Therefore, the above equation can be rewritten as:

$$S_{\text{specimen}} = \lim_{dT \rightarrow 0} \frac{dV}{dT} + S_{\text{copper}} \quad (16)$$

Electrical resistance  $r$  is measured by the dc four terminal method, in which a constant current  $I$  is applied to both ends of the specimen to measure and determine voltage drop  $dV$  between the same wires of the thermocouple by subtracting the thermo-electromotive force  $\varepsilon$  (EMF) between leads.

$$\varepsilon = dV - Ir \quad (17)$$

## **2.7 Determining thermal conductivity of bulk materials**

For measuring the thermal properties of bulk specimens in this work, we use the laser flash thermal diffusivity method (LFA) technique. In this technique, one face of a specimen is irradiated by a short (1 ms) laser pulse. An IR detector monitors the temperature rise of the opposite side of the specimen. The thermal diffusivity is calculated from the temperature rise versus time profile. The thermal conductivity is related to the thermal diffusivity via Equation 3. At high temperatures where the heat capacity is constant, the thermal diffusivity measurement essentially yields the thermal conductivity. The utility of this method demands fairly strict specimen preparation requirements, there is little flexibility in the specimen geometry (8 x 8 x 2 mm, and 6 x 6 x 2 mm in this work). Such requirements are stringent, in order to prevent the laser pulse to flash through and directly reach the IR detector.

The LFA 457 from Netzsch was used in this work. This bench-top instrument allows measurements from -125 °C to 1100 °C using two different interchangeable furnaces. The temperature increase in the back surface of the specimen can be measured at very low sub-ambient temperatures via infrared sensor technology. The instrument accommodates specimen sizes of 12 x 12 x 2 mm, 8 x 8 x 2 mm, and 6 x 6 x 2 mm, and the measurements can be run on 3 specimens in the meantime. In addition, the specimen surfaces should be highly emissive to maximize the amount of thermal energy transmitted from the front surface and to maximize the signal observed by the IR detector. Usually, this requires the application of a thin coating of graphite to the specimen surfaces, which is done manually in this work. If good adhesion is not achieved, this coating procedure can potentially be a source of significant error.

## 2.8 Experimental uncertainty

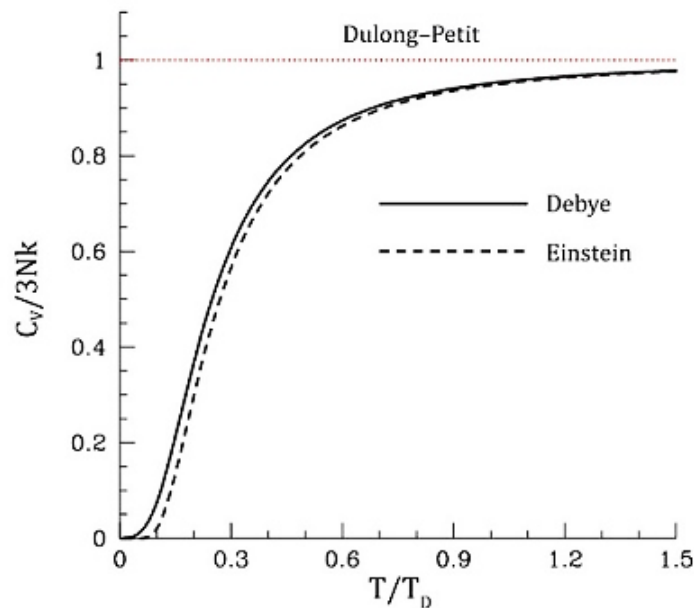


**Figure 17.**  $C_V/3Nk$  as a function of temperature as predicted by the Debye model and by Einstein's earlier model.  $C_V$  is heat capacity,  $N$  the atom number,  $k$  Boltzmann constant and  $T_D$  Debye temperature. The red line corresponds to the classical limit of the Dulong-Petit law.

Certain materials have been reported with  $ZT > 1.5$  [35, 36], but few have been confirmed by others, and no devices have been assembled that show the efficiency expected from such high- $ZT$  materials. The indigenous difficulty in thermoelectrics is that direct efficiency measurements require nearly as much intricacy as building an entire

device [28]. Thus practical appraisal of the  $ZT$  typically relies on measuring the individual contributing material properties.  $S$  and  $\sigma$  are measured by ZEM;  $\kappa$  is calculated from heat capacity, density along with thermal diffusivity, which is measured via LFA. The heat capacity of most systems is not a constant. Rather, it depends on the state variables of the thermodynamic system under study. In particular, it is dependent on temperature itself, as well as on the pressure and the volume of the system. For many solids composed of relatively heavy atoms whose atomic numbers are greater than iron, at non-cryogenic (much larger than the Debye temperature) temperatures, the heat capacity approaches  $3R = 24.94$  joules per kelvin per mole of atoms (Dulong–Petit law, 1819,  $R$  is the gas constant).

In thermodynamics and solid state physics, the Debye model treats the vibrations of the atomic lattice as phonons in a box, in contrast to the Einstein model, which treats the solid as many individuals, non-interacting quantum harmonic oscillators. As shown in Fig. 17, the Debye model correctly predicts the low-temperature dependence of the heat capacity, which is proportional to  $T^3$ . The Einstein model of the solid predicts the heat capacity accurately at high temperatures, while it noticeably deviates from experimental values at low temperatures. They are two models of the same thing, but of different scales. In this work, Dulong-Petit law is used to predict the heat capacity:

$$C_{P,m} \approx C_{V,m} \approx \frac{3Nk}{M} \quad (18)$$

where  $M$  is the mole mass. For HH alloy  $(Zr_{0.4}Hf_{0.6})NiSn$ ,  $N=3$  and  $(Zr_{0.4}Hf_{0.6})Ni_{1.15}Sn$ ,  $N=3.15$ . The volumetric mass density  $\rho$  is measured via Archimedes' principle, which can be formulated as follows:

$$\frac{\rho}{\rho_{\text{water}}} = \frac{m_{\text{air}}}{m_{\text{air}} - m_{\text{water}}} \quad (19)$$

where  $\rho_{\text{water}}$  is the density of water,  $m_{\text{air}}$  the mass measured in air and  $m_{\text{water}}$  the mass measured in water. The results of measurements of the TE properties can vary

considerably above room temperature, where thermal gradients in the measurement system would add to systematic inaccuracies. The uncertainty in  $ZT$  can be formulated as

$$\frac{\Delta ZT}{ZT} = 2 \frac{\Delta S}{S} + \frac{\Delta \sigma}{\sigma} + \frac{\Delta C_P}{C_P} + \frac{\Delta D}{D} + \frac{\Delta \rho}{\rho} \quad (20)$$

As a typical  $ZT$  measurement above room temperature requires the measurement of  $D$  (thermal diffusivity) with uncertainty of 5 % (LFA 457 from Netzsch), Seebeck coefficient and electric conductivity 7 % (ZEM-3 from ULVAC), density <1 % (DMA 5000 M from Anton Paar) and  $C_P$  <5 % (DSC), the uncertainty in  $ZT$  could reach 18 %. With calculations based on Dulong-Petit law and Archimedes' principle,  $\Delta ZT$  might extend to much higher than 18 %.

The accuracy of LFA is related to the fitting mode, and in this work, a Cowan model with pulse correction is chosen to fix the thermal diffusivity curve. It should be noticed that density is treated as a known condition, so the uncertainty of density measurement affects directly to the uncertainty of LFA measurement. Furthermore, small inhomogeneity (even < 5 %) can result in huge variations in TE properties within a specimen, making repeatability and combining results of different measurements laborious. In the case of sublimation, microstructural evolution, electrochemical reactions and phase transitions, reliable property values are particularly difficult to obtain. Even the act of measuring a specimen at high temperatures itself can alter its properties. In this work, the measurement of each specimen is three times repeated to avoid inaccuracies.

## 2.9 Procedures

(Zr<sub>0.4</sub>Hf<sub>0.6</sub>)Ni<sub>1+x</sub>Sn ( $x = 0, 0.2, 0.5, 0.8$  and  $0.15$ ) ingots were synthesized in an arc-melting furnace under argon atmosphere by melting a mixture of Zr (purity 99.8 %), Hf (99.9 %), Ni (99.95 %) and Sn (99.99 %) with molar ratios of Zr:Hf:Ni:Sn = 0.4:0.6:1+x:1. These ingots were melted back and front four times to ensure the homogeneity. The melted ingots solidify very quickly inside a water-cooled copper hearth plate mold. This process eliminates ingot macro-segregation and significantly reduces micro-segregation, improving thermoelectric properties. The majority of the quenched ingots were grounded to powders using vibration disc mill (specimen AM), and sintered

at 1623 K for 8 min under pressure of 50 MPa in an Ar atmosphere by employing the spark plasma sintering (SPS) technique (specimen AS). After SPS, aging was performed in a glass tube furnace at 1173 K for 2 days under an argon atmosphere (specimen ASA2D), 1 week (specimen ASA7D) and 4 weeks (ASA28D), subsequently furnace cooling. Aging for 1 week was also carried out for the rest of the arc-melted and quenched ingots (specimen AMA7D).

To control the chemical composition of the specimens, inductively coupled plasma (ICP) spectrometry was used. The crystalline phases of the specimens were determined by powder X-ray diffraction (XRD) measurements, using a silver anode with a Ge (111) monochromator and capillaries with a diameter of 0.3 mm. The transport properties electrical conductivity  $\sigma$  and the Seebeck coefficient  $S$  were measured by using ZEM3 (ULVAC) and thermal diffusivity was by LFA 457 (Netzsch). EDX analysis was performed with an accelerating voltage of 15 keV. Rietveld refinements were carried out mainly with a fully occupied 4c sublattice of HH with Ni. For AM specimen which lacks homogenizing process, Rietveld refinements were performed based on a disordered HH matrix.

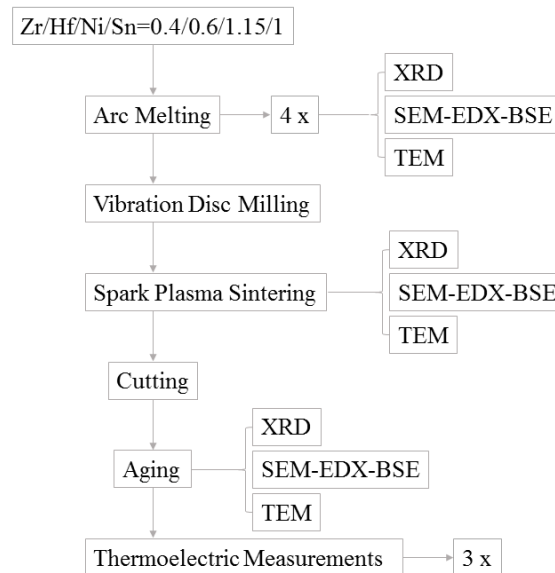


**Figure 18.** Scheme of experimental procedures.

## 3. Results and Discussions

### 3.1 ICP-MS

Inductively coupled plasma mass spectrometry (ICP-MS) was used to determine the chemical composition of AM and AS  $Zr_{0.4}Hf_{0.6}Ni_{1.15}Sn$  specimens. The results are shown in Tab. 1. It is noted that significant reduction of Sn and Ni amounts reported by Sekimoto *et al.* [37] was not observed after AM and SPS process. As expected, the (ZrHf)/Sn ratio approached 1 and Ni/Sn 1.15 indicating that the synthesis of the compounds was successful.

**Table 1.** ICP analysis of nominal composition  $Zr_{0.4}Hf_{0.6}Ni_{1.15}Sn$ \*.

	(ZrHf)/Sn	Ni/Sn
(ZrHf)Ni <sub>1.15</sub> Sn (AM)	0.972 ±0.037	1.15 ±0.062
(ZrHf)Ni <sub>1.15</sub> Sn (AS)	0.965 ±0.024	1.146 ±0.055

\*ICP Analysis was performed by Gerhard Werner from MPI Stuttgart.

### 3.2 XRD

**Table 2.** Quantitative phase analysis.

	HH (at. %)	H (at. %)
AM	95.7	4.3
AMA7D	87.4	12.6
AS	91.4	8.6
ASA7D	82.6	17.4

**Fig. 19** shows powder XRD patterns of  $(Zr_{0.4}Hf_{0.6})Ni_{1.15}Sn$  (aging time  $t = 0$  and 168 h) specimens. The obtained powder patterns showed mainly reflections originating from the HH phase along with a small amount of H second phase. The exception is AS specimen, the first reflection at low  $2\theta$  value indicates an impurity, whose reflection-intensity is reduced dramatically after 168 h of aging. The changes in reflection intensities

at  $2\theta = 14.6^\circ$  indicates an increased amount of H phase during aging. A clear correlation between aging time and phase amount of H phase was observed, indicating the H phase as the thermodynamically stable one. Extended aging is beneficial to the formation of Ni clusters. The quantitative phase analysis is listed in **Table 2**. The phase separation between H and HH phases can be explained by the spinodal decomposition, while the growth of the H phase could be initiated from Ni-rich clusters through diffusion of Ni atoms from the neighboring areas into the vacant sites in the matrix [38, 39]. The higher the potential of the clustering of Ni atoms, the more possible the formation of the H second phase.

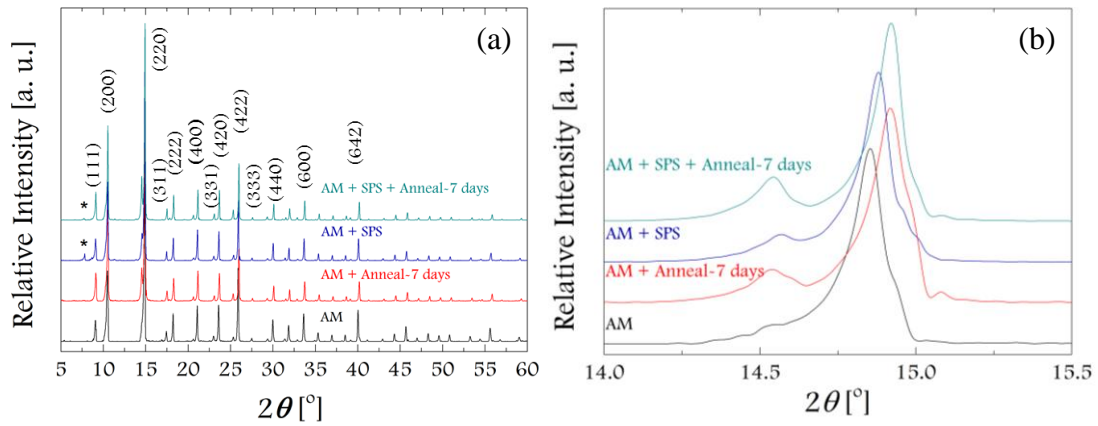


**Figure 18.** Refined powder XRD patterns (\* indicates impurity peaks). The measurement was carried out with Ag-K $\alpha_1$  radiation (0.55941 Å) with a Ge (111) monochromator at room temperature.

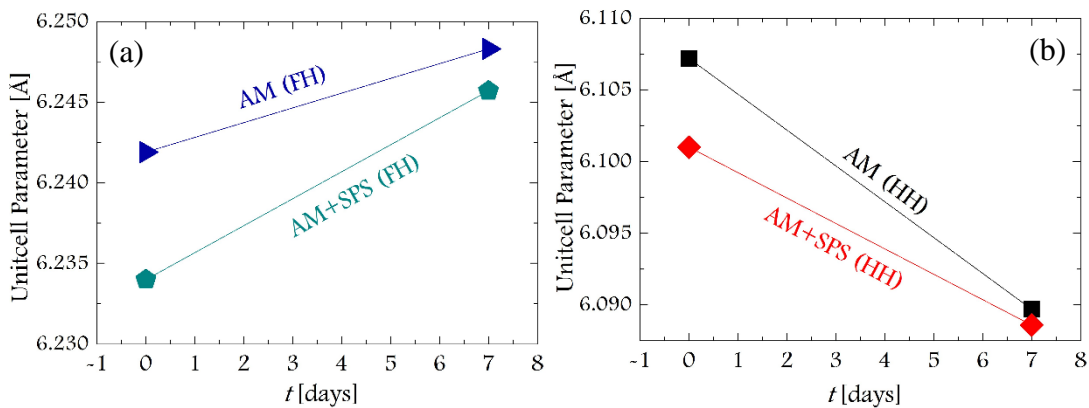


**Figure 20.** (a) Lattice parameter evaluated by refining the Heusler and (b) half-Heusler reflections.

As shown in **Fig. 20**, the lattice parameter of HH phase decreases with increasing aging time  $t$  while the lattice parameter of the H phase increases, due to: (i) the enrichment

of excess Ni atoms within the H phase during aging; (ii) the decrease of crystal disorders and defects during aging which reduces the lattice parameter; (iii) the different thermal expansion coefficients and E-modulus of H and HH phases.

### 3.3 Microstructure Analysis

#### 3.3.1 AM Specimens

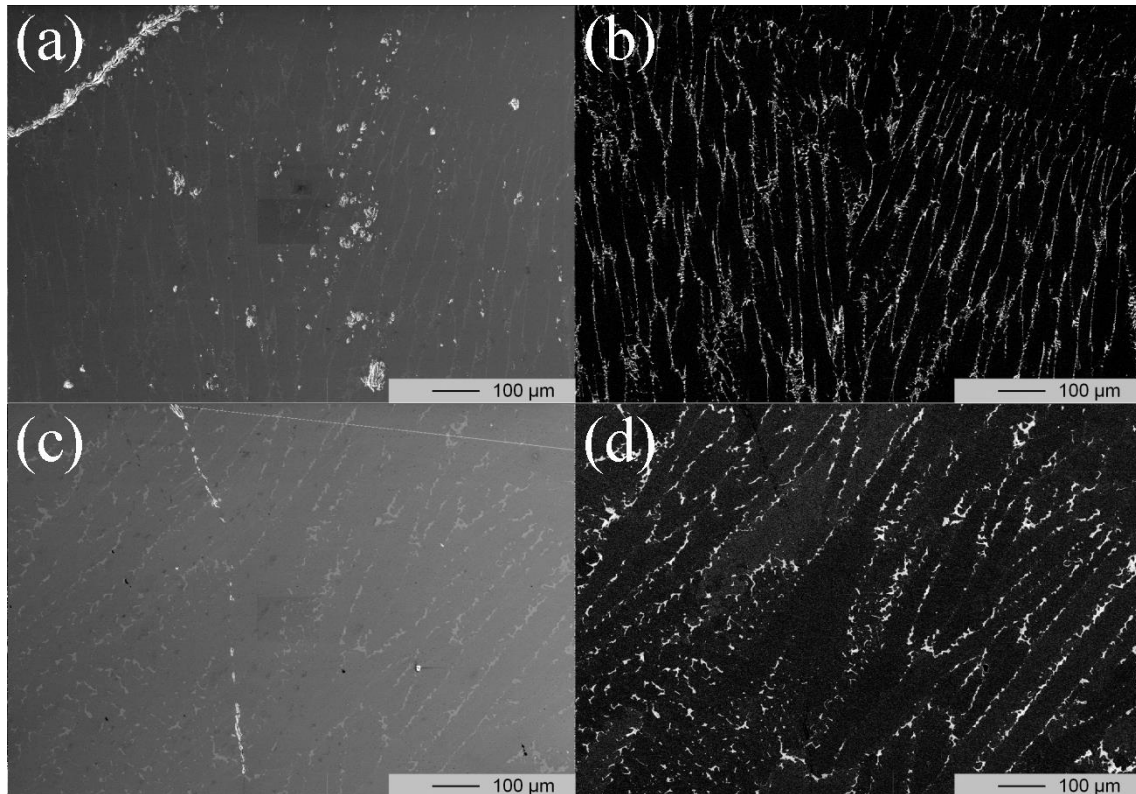


**Figure 21.** (a) SE and (b) BSE images of 0 % excess Ni AM specimens; (c) SE and (d) BSE images of 15 % excess Ni AM specimens.

As shown in **Fig. 21**, the specimens have uniform microstructure after solidification, which is composed of cellular dendrites a few hundred micron. No cracks were observed along the grain / sub-grain boundaries. During arc-melting, the heat source interacts with the material. The severity of thermal excursions does not vary from region to region in small dimensional specimens, which results in homogeneous fusion zones. The followed quench process induces preferred orientations of the solidification microstructure. Dendrites favor to orient along the temperature gradient.

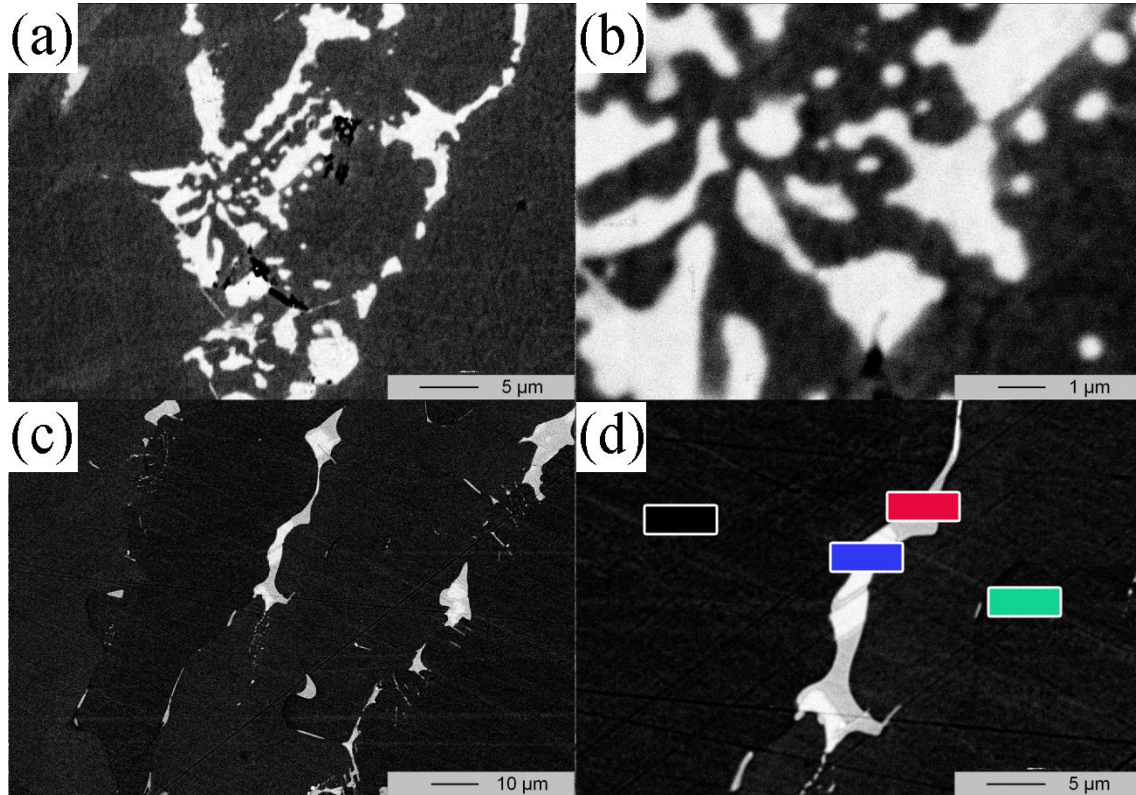


**Figure 22.** BSE images of (a-b) 0 % excess Ni AM specimens (c-d) 15 % excess Ni AM specimens.

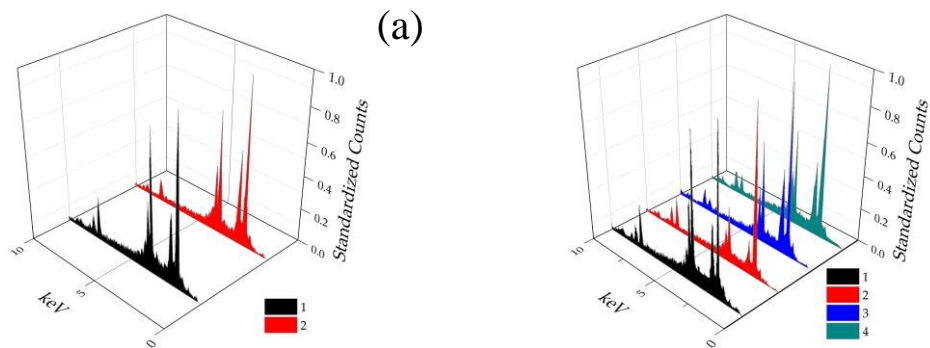


**Figure 23.** EDX analysis of phases in (a) Fig. 22b and (b) Fig. 22d. In (a): (1)  $Zr_{34.1}Hf_{23.37}Ni_4Sn_{38.53}$  ( $\gamma = 40.07$ ) and (2)  $Zr_{19.33}Hf_{17.67}Ni_{29.67}Sn_{33.33}$  ( $\gamma = 37.64$ ). In (b): (1)  $Zr_{20.40}Hf_{17.93}Ni_{29.76}Sn_{31.91}$  ( $\gamma = 37.60$ ), (2)  $Zr_{24.79}Hf_{19.58}Ni_{24.52}Sn_{31.11}$  ( $\gamma = 38.07$ ), (3)  $Zr_{34.38}Hf_{22.93}Ni_{9.61}Sn_{33.08}$  ( $\gamma = 39.45$ ) and (4)  $Zr_{18.33}Hf_{27.69}Ni_{34.64}Sn_{19.34}$  ( $\gamma = 38.38$ ).  $\gamma$  is the intensity of the signal of a phase, which can be calculated from  $\gamma = \sum_{i=1}^x a_i \eta_i$ , where  $a_i$  is atomic concentration,  $x$  the number of the phases and  $\eta$  the BSE coefficient taken from [40].

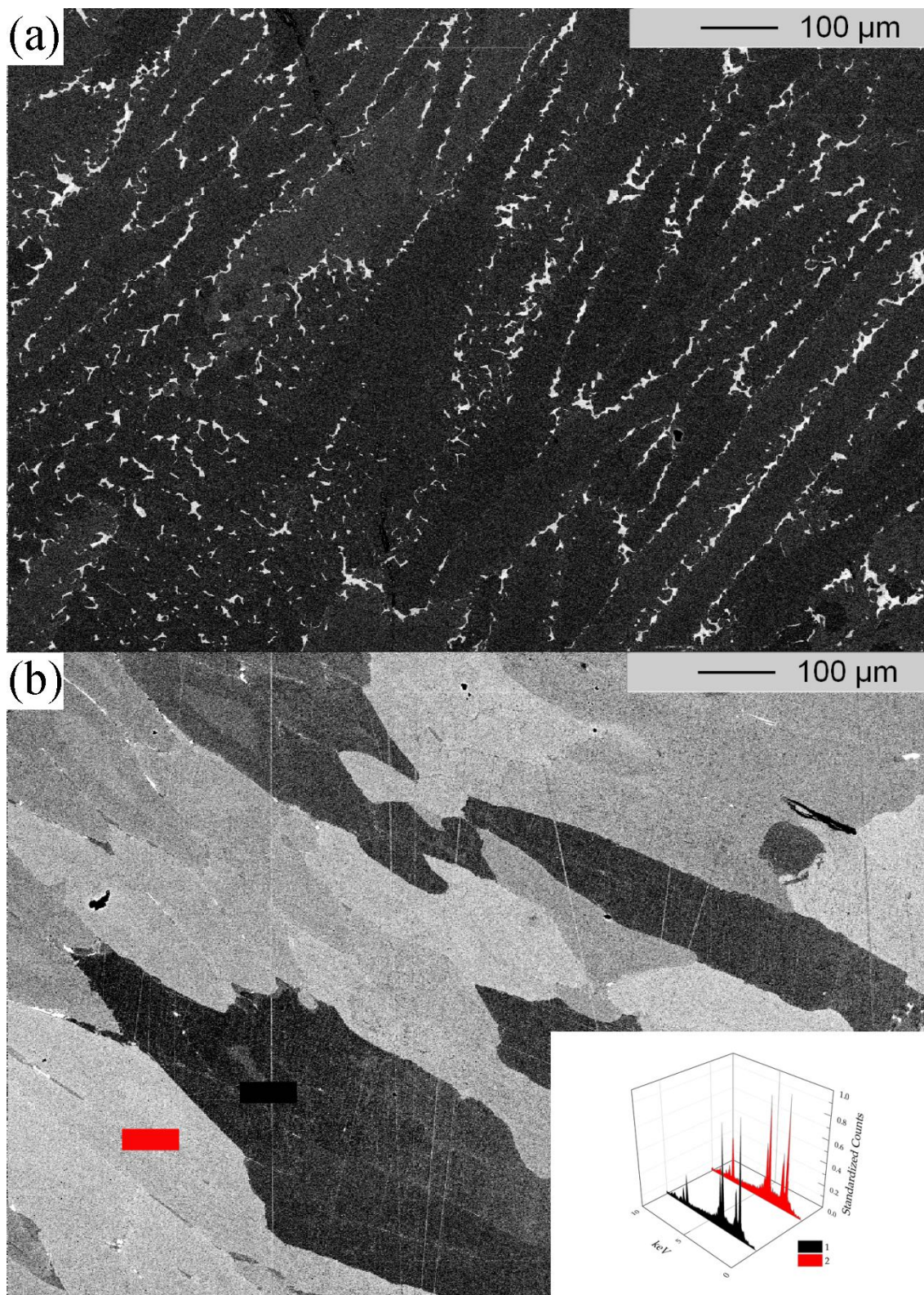


**Figure 24.** BSE images (a) 15 % AM and (b) 15 % AMA7D specimens. The result of EDX analysis is described as follows: (1) Near H phase  $Zr_{15.68}Hf_{12.33}Ni_{42.66}Sn_{29.33}$  ( $\gamma = 36.10$ ), (2) HH phase  $Zr_{19.02}Hf_{15.73}Ni_{32.35}Sn_{32.90}$  ( $\gamma = 37.25$ ).

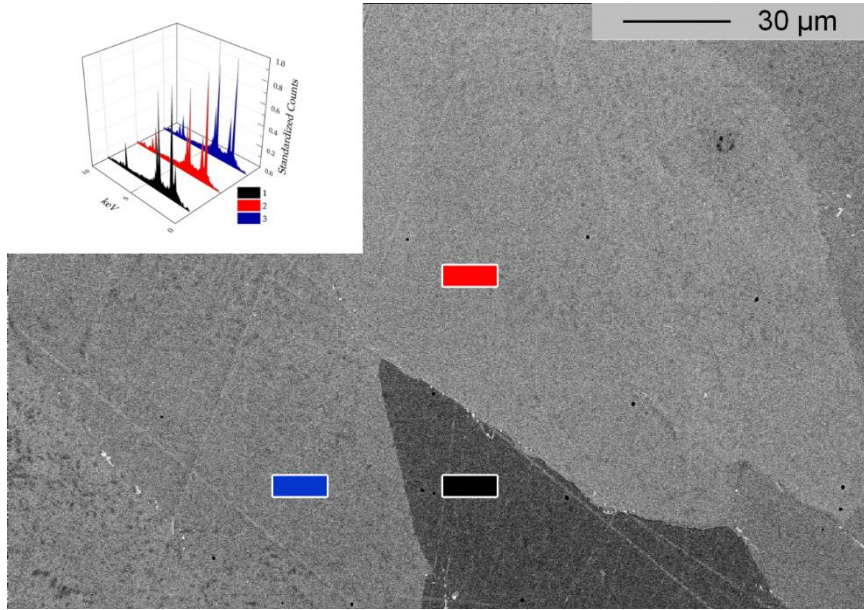


**Figure 25.** The BSE contrast due to the concentration fluctuation of Zr and Hf in 15 % AMA7D specimen. The result of EDX analysis is described as follows: (1)  $Zr_{32.06}Hf_{4.85}Ni_{28.23}Sn_{34.85}$  ( $\gamma = 36.23$ ), (2)  $Zr_{20.20}Hf_{18.10}Ni_{29.57}Sn_{32.14}$  ( $\gamma = 37.51$ ), (3)  $Zr_{20.25}Hf_{17.56}Ni_{29.57}Sn_{32.62}$  ( $\gamma = 37.46$ ).

At higher magnifications (**Fig. 22**), at least two different phases in 0 % AM and four phases in 15 % AM specimens were observed. To exactly determine the phase distribution, EDX was used to examine the multiphase-areas in specimens. As described in **Fig. 23a**, the composition contrast of  $Zr_{0.4}Hf_{0.6}NiSn$  specimen is formed by the bright Ni-poor phase  $Zr_{34.1}Hf_{23.37}Ni_4Sn_{38.53}$  and the dark near HH phase  $Zr_{19.33}Hf_{17.67}Ni_{29.67}Sn_{33.33}$ . In 15 % excess Ni system, the microstructure is much more complicated. As shown in **Fig. 23b**, the microstructure consists of at least four parts: (i) the darkest near-HH  $Zr_{20.40}Hf_{17.93}Ni_{29.76}Sn_{31.91}$ ; (ii) the Zr/Hf-rich  $Zr_{14.33}Hf_{32.71}Ni_{27.05}Sn_{25.91}$  phase; (iii) the brightest Ni-poor  $Zr_{34.38}Hf_{22.93}Ni_{9.61}Sn_{33.08}$  phase, and (iv) the near- $(ZrHf)_2Ni_2Sn$  phase  $Zr_{18.33}Hf_{27.69}Ni_{34.64}Sn_{19.34}$ . Notably, according to the stoichiometry, another Ni-rich phase should exist. Powder XRD patterns show the reflections originating only from H and HH phases, suggesting that concentrations of impurity phases are too low or the accuracy of EDX spectrum is not high enough. X-rays can be generated by any atom that is sufficiently excited by the incoming beam. These X-rays are emitted in many directions, and they may not all escape from the specimen. The probability of X-rays escaping from the specimen and being detected depends on the energy of X-rays, the amount, and density of material. EDX can only analyze a very

limited area of the specimen, for an inhomogeneous part of the specimen, the results of EDX can only be regarded as an evidence of multiphase.

The contrast of image **Fig. 24a** comes from the atomic number contrast of different phases rather the preferred orientations of crystals. This can be confirmed by the calculated  $\gamma$  value of each phase. The higher the  $\gamma$  value, the brighter the phase is. These values match well with the BSE images. As shown in Fig. 24b, after 168 h aging at 1173 K, the microstructure is more homogenous compared with AM specimens. The intermetallic impurities demonstrated in **Fig. 23** reduced drastically after aging. The contrast of the BSE image mainly comes from the Zr/Hf concentration fluctuations in HH phase (**Fig. 25**). For ZrNiSn and HfNiSn dissolve totally with each other, artificially it is hard to design these two phases in a certain area. All of three phases have chemically near-HH compositions with different ratios of Zr and Hf concentrations, i.e. concentration fluctuations in  $4a$ -sublattice.

### 3.3.2 AS Specimens

As shown in **Fig.26** and **Fig. 27**, microstructures of AS specimens were split by vibration milling and spliced by SPS. There are more interfaces existing and different phases are separated in small units divided by interfaces. At these interfaces, the existence of low/high-angle grain boundary dislocations or antiphase boundaries (APB) is highly possible. To confirm this argument, TEM examination is essential. The long-range diffusion of atoms can be affected by these interfaces. Estimated by statistic methods, the approximate statistic grain size  $d$  is graphically determined and listed below.

**Table 3.** *The impact of aging on grain sizes.*

	$d$ [ $\mu\text{m}$ ]
AS	24.88
ASA2D	11.04
ASA7D	6.79
ASA28D	5.99

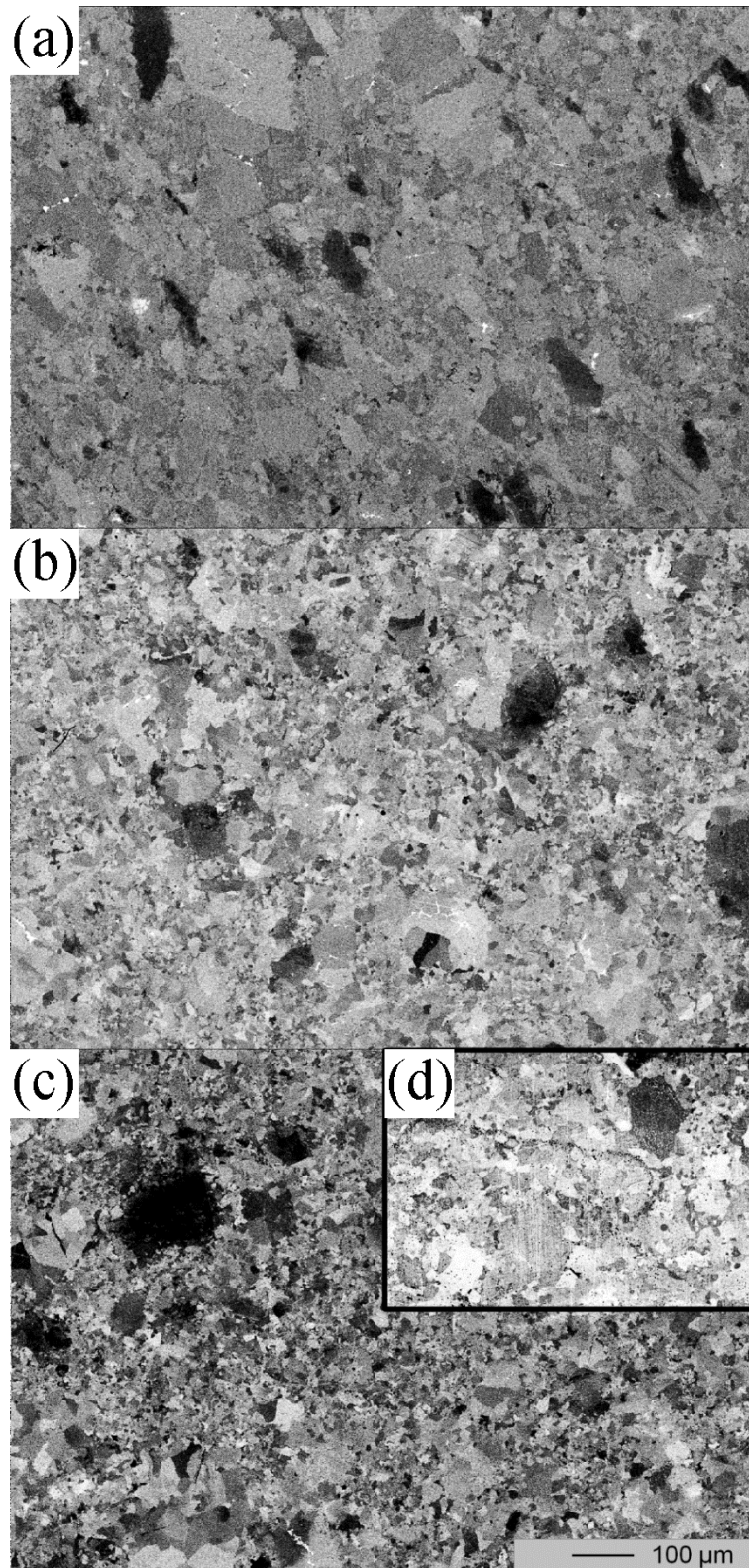


**Figure 26.** BSE images of specimens (a) AS (b) ASA2D (c) ASA7D and (d) ASA28D.

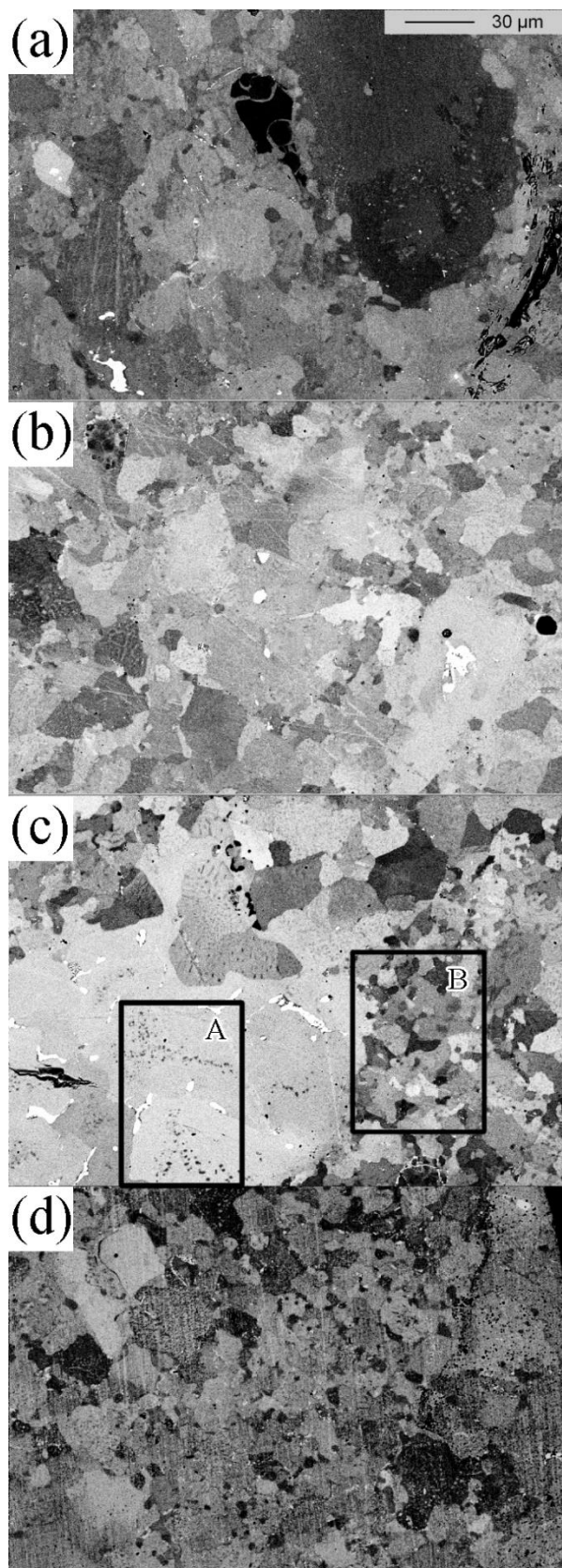


**Figure 27.** BSE images of specimens (a) AS (b) ASA2D (c) ASA7D and (d) ASA28D at higher magnification.

During the SEM examinations, the operator has tried to take the most representative images. Whether these micrographs can represent the whole microstructure? This question could be answered by features of the synthesis process and the thermoelectric measurement results. The AM specimens were disc milled and sintered, so it can be assumed that the specimen for the SEM observation was well mixed. After aging, the thermal conductivity of specimens decreases dramatically, which be explained by the great increase of scattering centers or boundaries.

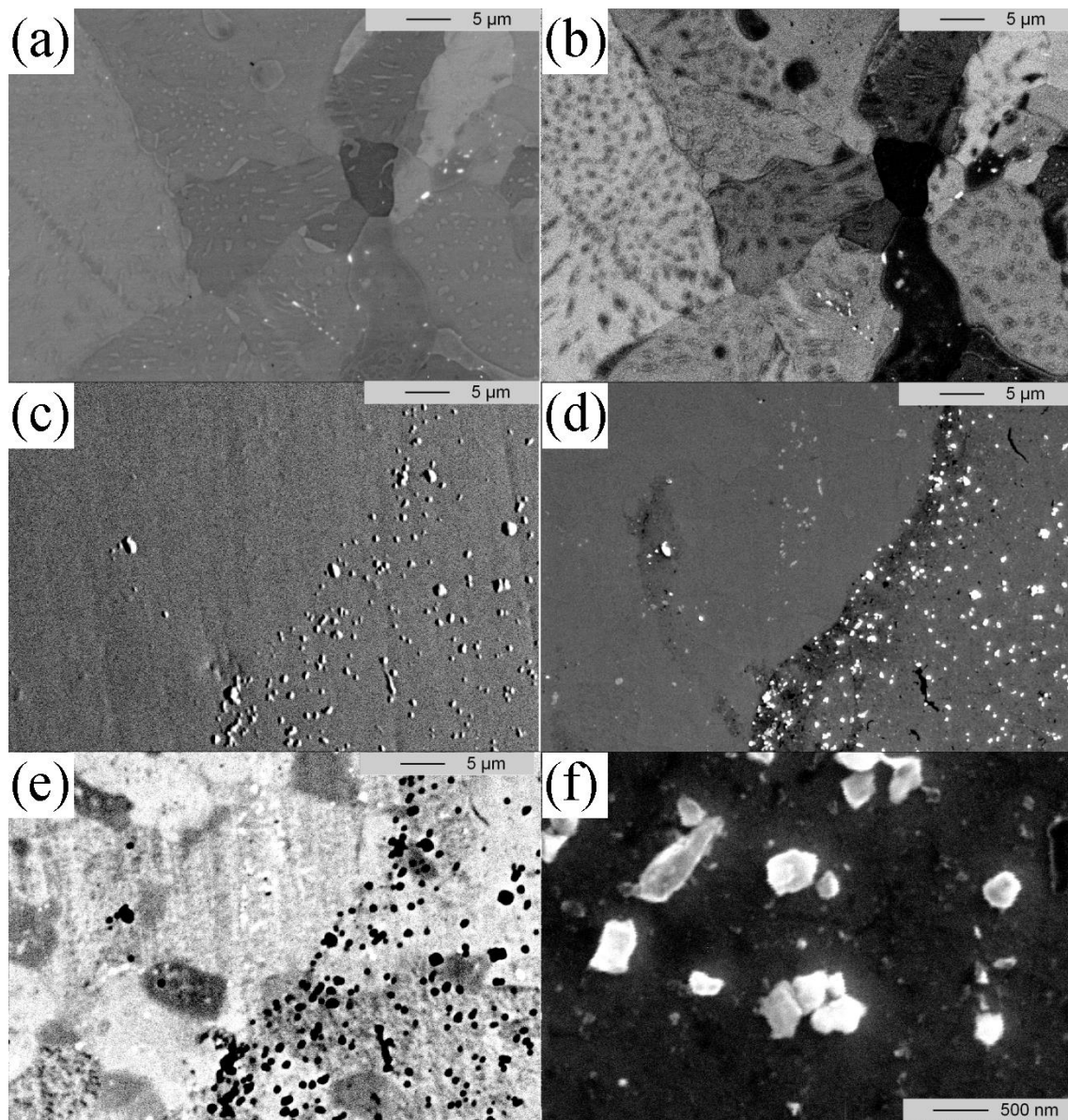


**Figure 28.** Submicron precipitates in (a-b) ASA7D and (c-f) ASA28D specimens.

Generally, the refinement of the microstructure can be achieved by recrystallization or phase transitions [41]. Recrystallization cannot be accomplished

without plastic deformation energy [42]. For AS specimens were sintered under 50 MPa pressure via SPS, the plastic deformation energy could be reserved after the 8 min heat treatment. Also, phase transitions can be involved in our specimens. **Fig. 27c** shows the microstructure of ASA7D specimen: a mixture of fine and coarse grains with micron-dispersions located inside grains or at grain boundaries. This microstructure leads to lower thermal conductivity compared with the ASA2D specimen, on which different microstructure was observed (**Fig.27b**). The microstructure in area B in **Fig. 27c** is retained in **Fig. 27d** while the microstructures in area A in **Fig. 27c** disappeared after longer time aging. At a higher magnification, as shown in **Fig. 28a-b**, submicron precipitates were observed within the grains. **Fig. 29** proves that these precipitates are rich in Ni. This kind of Ni enrichment takes place not only within grains but also at the grain boundaries. Coupled with XRD analysis data, a Ni-rich second phase can only be identified as the H phase.

After 672 h aging, submicron particles are attached on the surface of the polished section (**Fig. 28c-f**). Specimens were polished again without diamond suspension, subsequently flushed and dried. The same observation was obtained, suggesting that these particles were not induced during preparation. As these particles distributed inhomogeneously in small areas and also in the interior of the specimen, the possibility of oxides can be excluded. A possible explanation for this observation could be: these particles come from grain boundary planes that are parallel to the surface of the section. After preparation, these particles remain attached on the surface of specimens.

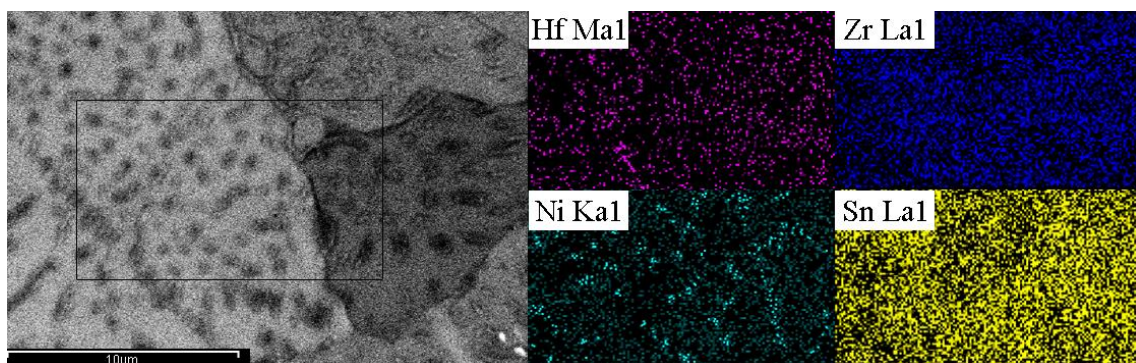


**Figure 29.** EDX mapping proves Ni enrichment in the precipitation regions of ASA7D specimen.

### 3.3.3 Fracture Surface Analysis

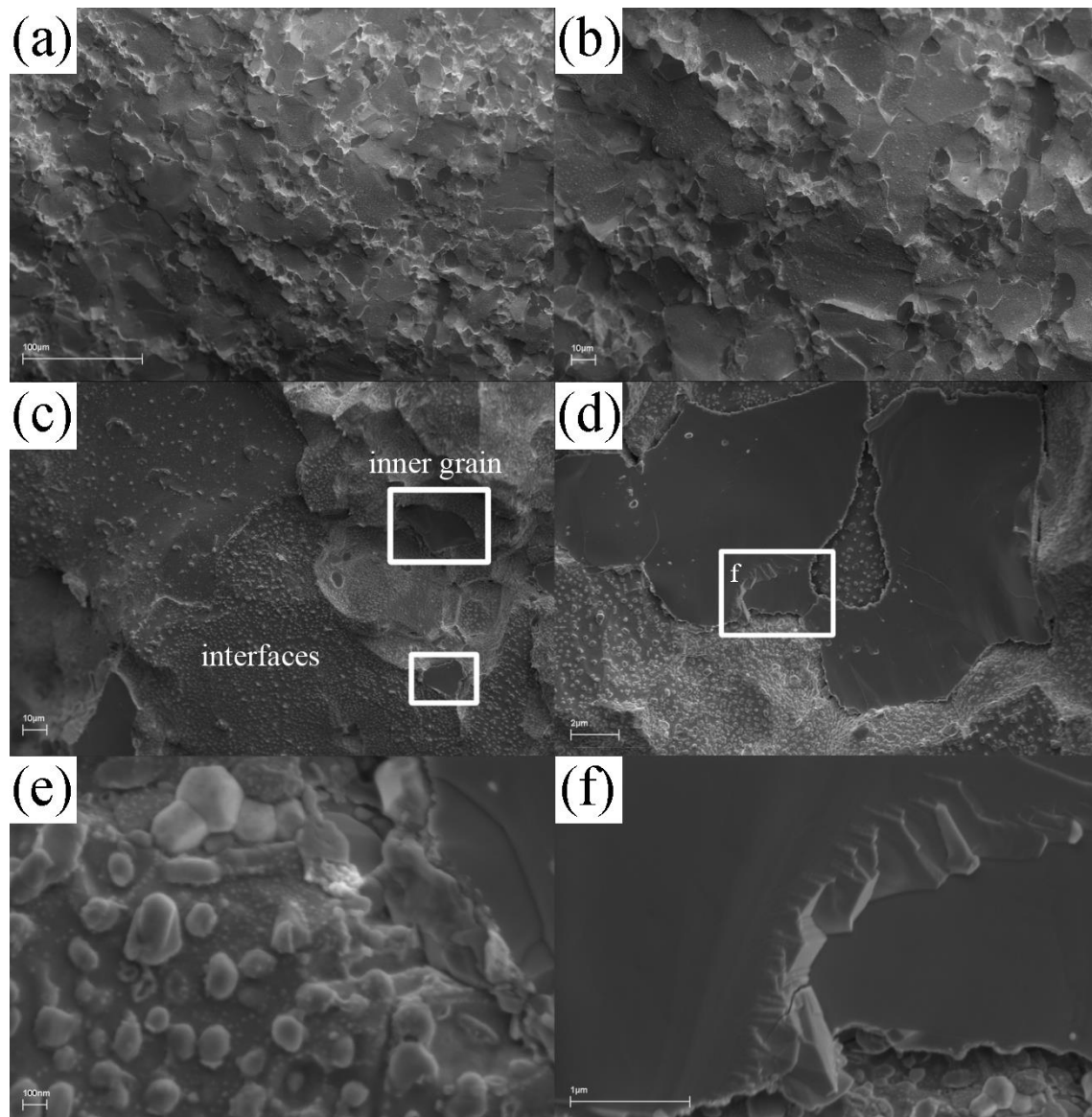


**Figure 30.** Brittle fracture section of ASA2D specimen.

Fractography of the ASA2D specimen is shown in **Fig. 30**. **Fig. 30a-b** give an overview of the fracture structure. The **Fig. 30c** provide the criteria to assess whether the fracture is trans- or intercrystalline. **Fig. 30f** indicates the fracture of the specimen was brittle. Precipitates of ca. 100 nm were observed at the interfaces rather within grains (**Fig. 30d** and **Fig. 30f**).

Fractography of the ASA7D specimen is shown in **Fig. 31**. The highlight region in **Fig. 31** indicates the transcrystalline fracture. Submicron precipitates are bound with

the river lines, indicating that a precipitation-hardening effect may work. Notably, submicron precipitates were observed both at interfaces and within grains in ASA7D specimen, while no or few precipitates within grains in ASA2D specimen.

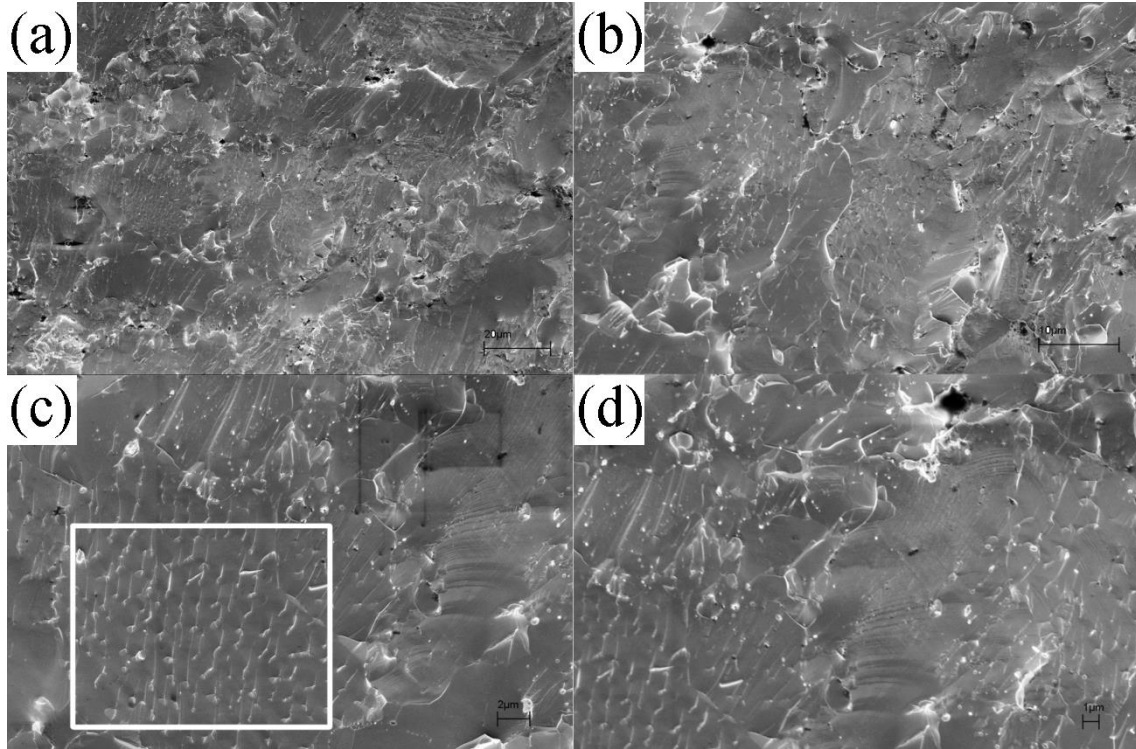


**Figure 31.** Brittle fracture section of ASA7D specimen.

### 3.3.4 Model for Microstructure Evolution

As mentioned before, the H phase prefers to precipitate primarily at interfaces, due to the low nucleation energy barrier there. Excess Ni atoms departed from the interstitial positions of HH matrix to a more energy-convenient position to construct the H phase by long-range diffusion (**Fig. 32**). Interfaces act as excess Ni sinkers. Till the local concentration of Ni atoms is high enough, the driving force for diffusion will be trivial and the precipitation within grains becomes possible. In HH phase alloys, energy-convenient positions can be antisite defects, vacancies as revealed in **Fig. 33** and dislocations.

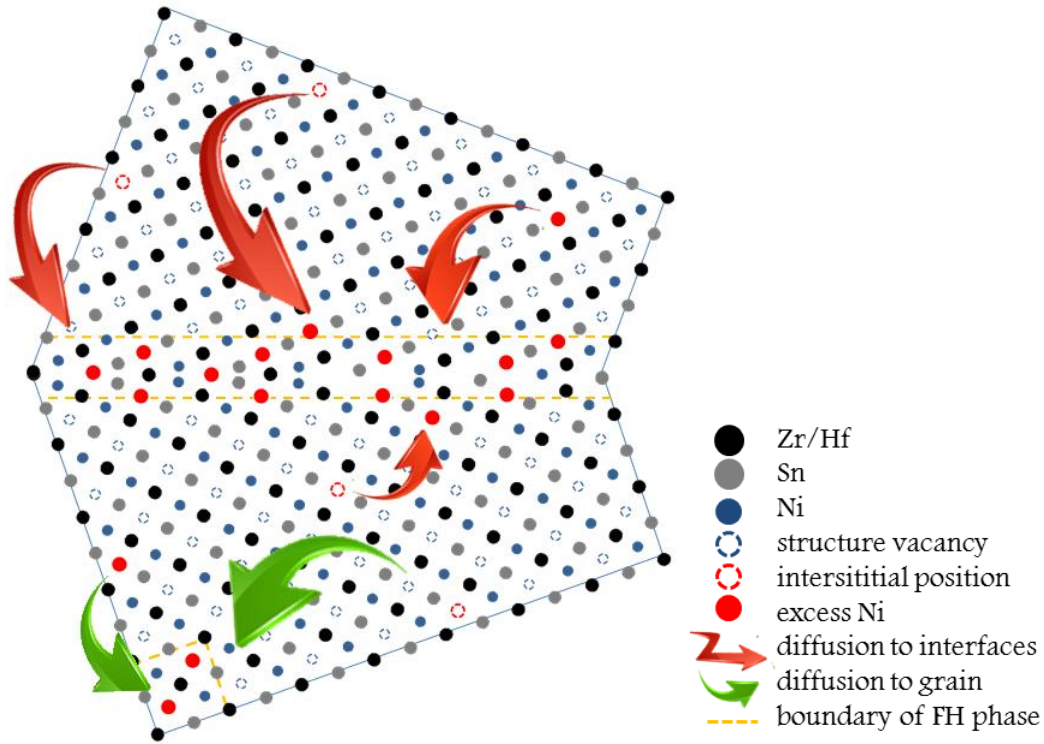


*Figure 32. Modeling for microstructure evolution.*

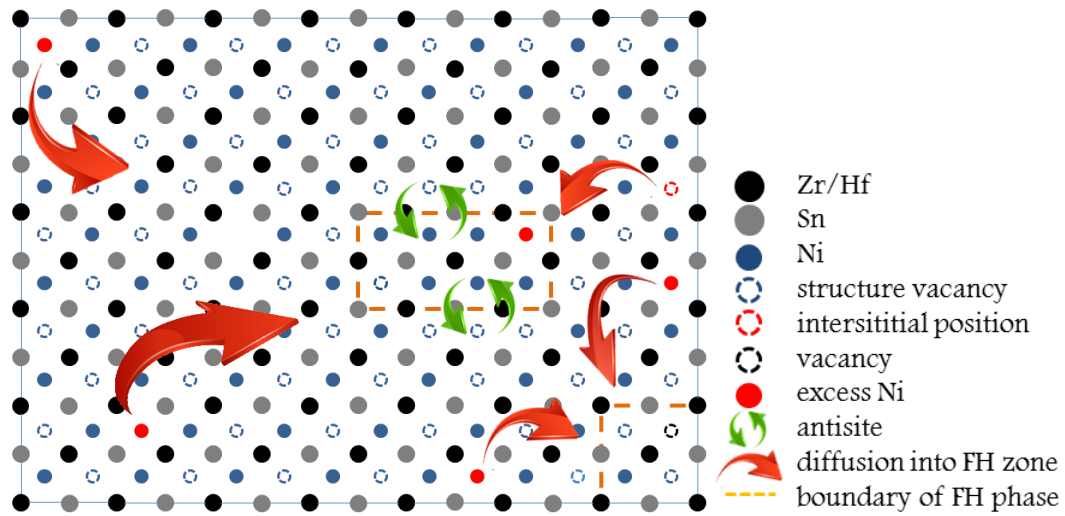


*Figure 33. Modeling for phase separation.*

### 3.3.5 Thermoelectric Properties

The electrical conductivity increases with increasing temperature (**Fig. 26a**), showing typical semiconductor conduction behavior. After aging, the specimens have a much lower electrical conductivity. Without Hall-effect measurement, it is not possible to speculate whether this effect is due to a reduction in charge carrier concentration or the

carrier mobility. Without carrier concentration and mobility data, it is impossible to calculate effective mass and relaxation time of the charge carriers or to quantitative analyze the scattering effect of precipitates.

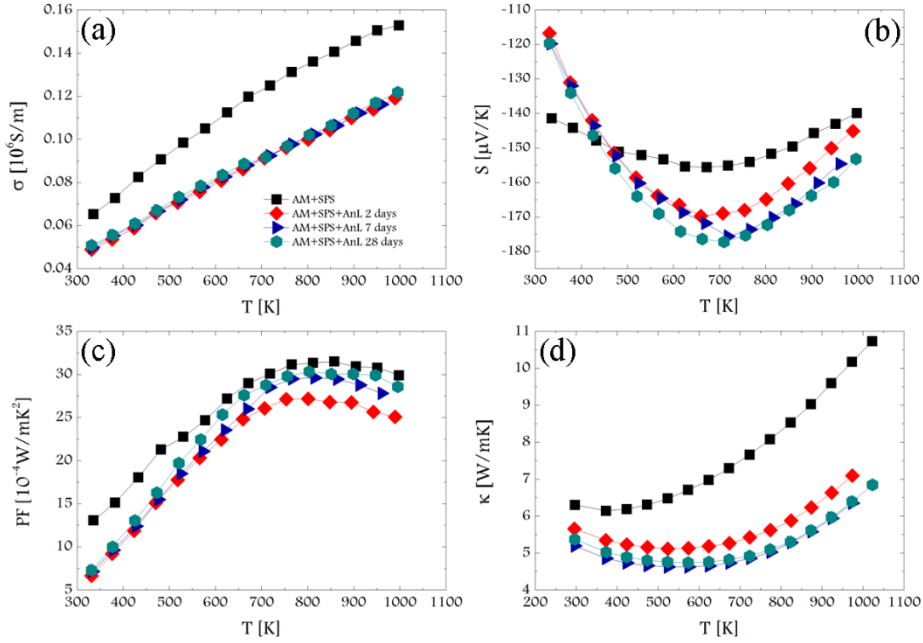


**Figure 34.** Temperature dependence of (a) electrical conductivity, (b) Seebeck coefficient, (c) power factor and (d) thermal conductivity of  $Zr_{0.4}Hf_{0.6}Ni_{1.15}Sn$  alloys.

The temperature dependence of the Seebeck coefficient  $S$  of the HH material is described in **Fig. 34**. The negative sign of the Seebeck coefficients indicates dominant n-type conduction in these specimens. Notably, the Seebeck coefficient increases with the aging time  $t$ . Again, the Hall-effect measurement is the key for further discussing this trend based on Equation 10. The Energy filtering effect may play a role in this alloy system by considering the size of the precipitates [43]. Moreover, the close connection between aging time and  $S$  may indicate a change of the band gap. By using Goldsmid–Sharp formula [44] and Arrhenius fitting [45], the band gap at the region of transition from heavily doped to intrinsically semiconducting behavior and the intrinsic band gap are obtained respectively. As shown in **Fig. 35**, the Goldsmid–Sharp band gap calculated from  $S$  rises slowly due to the aging and stays constant after 168 h. Distinctly, the intrinsic band gap calculated from electrical conductivity drops persistently with increased aging time, which matches with the fact that the metallic H phase increases with the aging time.

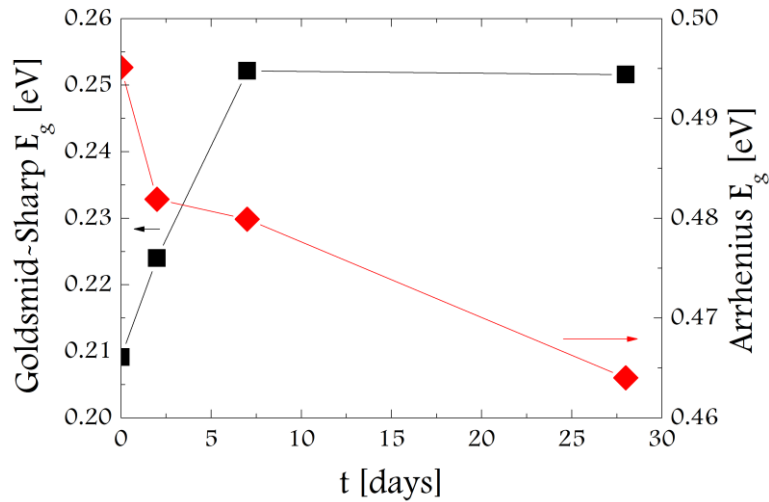


**Figure 35.** Band gap calculation with the Goldsmid–Sharp formula and Arrhenius fitting.

Owing to the high electrical conductivity, the AS specimen possesses a higher power factor. The carrier thermal conductivity is calculated with the Wiedemann–Franz relationship with a Lorentz number of  $2.0 \times 10^{-8} \text{ V}^2\text{K}^{-2}$ . The lattice thermal conductivity is obtained by subtracting the carrier thermal conductivity from the total thermal conductivity. As shown in **Fig. 36a**, the lattice thermal conductivity of the AS specimen is larger, which can be explained by the lack of phonon scattering centers, i.e. H phase precipitates. During aging, these precipitates grew up and reached the submicron scale after 168 h. The specimen after 672 h aging possesses the lowest  $\kappa_L$  indicating that the grown-up precipitates scatter the phonons more effectively.

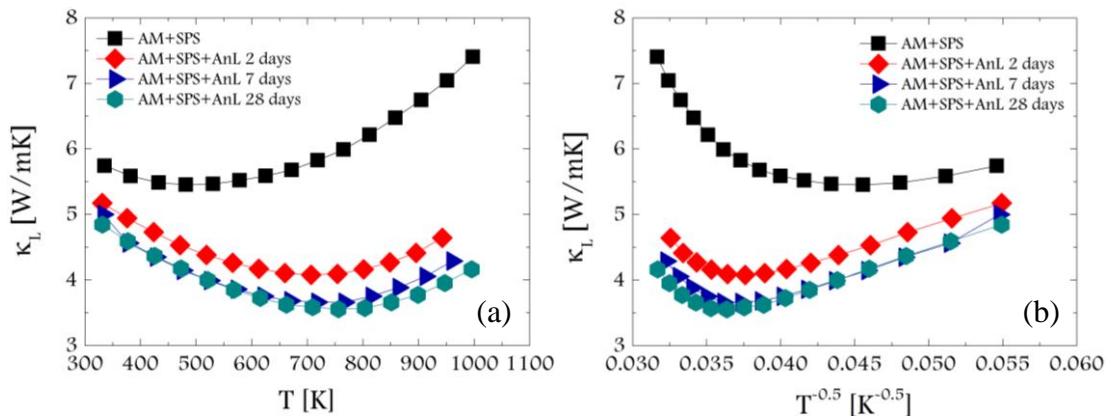


**Figure 36.** Temperature dependence of lattice thermal conductivity.

Below 700K, the lattice thermal conductivity is well proportional to  $T^{-0.5}$ , indicating the alloy and boundary scattering dominates below in all of the aged specimens (**Fig. 36**). With increased aging time, this kind of domination is pushed to higher temperatures. Above 700K (or higher), Umklapp and electron-phonon mechanisms take charge and the  $T^{-0.5}$  dependence of  $\kappa_L$  deviates from the linear relationship. The ratio of electrical conductivity to the total thermal conductivity is calculated in **Fig. 37a**. This ratio increases with increasing aging time indicating that the submicron structure in the aged systems can relatively constrain phonon transport without greatly deprecating the electrical transport. As a result, a more than 50% improvement of  $ZT$  value on the unaged specimen was achieved (**Fig. 37b**).

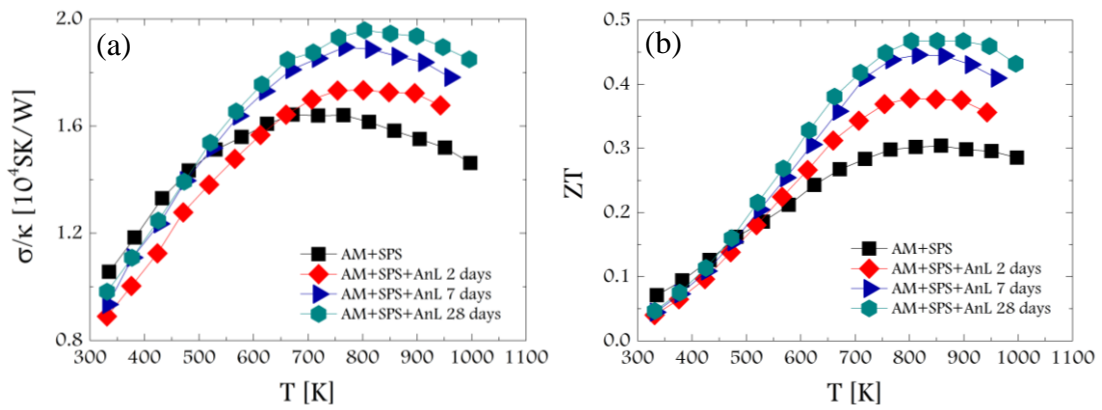


**Figure 37.** (a) The ratio of electrical conductivity and total thermal conductivity and (b) figure of merit of  $Zr_{0.4}Hf_{0.6}Ni_{1.15}Sn$  alloys.

## **4. Conclusion**

Spinodal half-Heusler  $\text{Zr}_{0.4}\text{Hf}_{0.6}\text{Ni}_{1.15}\text{Sn}$  thermoelectrics was synthesized and aged. Microstructural and thermoelectric examinations were performed. The spinodal phase decomposition and growth was found to be the driving force for the microstructure evolution. A new model is proposed to explain the formation of H phase and the Ni clustering. H phase precipitates during aging effectively reduce the thermal conductivity, increase the Seebeck coefficient and improve the thermoelectric performance of alloys. As a result, a more than 50 % improvement of the  $ZT$  value on the unaged specimens was achieved. Detailed control of the distribution of Ni can be the key to further improve thermoelectric properties of the half-Heusler thermoelectrics.

## References

- [1] W. Jeischoko, *Metall. Trans. A* 1 (1970).
- [2] D.M. Rowe, CRC handbook of thermoelectrics, CRC press 1995.
- [3] H. Hazama, M. Matsubara, R. Asahi, T. Takeuchi, *J. Appl. Phys.* 110(6) (2011) 063710.
- [4] H. Hazama, M. Matsubara, R. Asahi, *J. Electron. Mater.* 41(6) (2012) 1730-1734.
- [5] J.E. Douglas, P.A. Chater, C.M. Brown, T.M. Pollock, R. Seshadri, *J. Appl. Phys.* 116(16) (2014) 163514.
- [6] J.E. Douglas, C.S. Birkel, M.-S. Miao, C.J. Torbet, G.D. Stucky, T.M. Pollock, R. Seshadri, *Appl. Phys. Lett.* 101(18) (2012) 183902.
- [7] C.S. Birkel, J.E. Douglas, B.R. Lettiere, G. Seward, N. Verma, Y. Zhang, T.M. Pollock, R. Seshadri, G.D. Stucky, *Phys. Chem. Chem. Phys.* 15(18) (2013) 6990-6997.
- [8] S. Ögüt, K.M. Rabe, *Phys. Rev. B* 51(16) (1995) 10443.
- [9] J. Tobała, J. Pierre, *J. Alloys Compd.* 296(1) (2000) 243-252.
- [10] J. Tobała, J. Pierre, S. Kaprzyk, R. Skolozdra, M. Kouacou, *J. Phys. Condens. Matter* 10(5) (1998) 1013.
- [11] F. Casper, T. Graf, S. Chadov, B. Balke, C. Felser, *Semicond. Sci. Technol.* 27(6) (2012) 063001.
- [12] S. Chen, Z. Ren, *Mater. Today* 16(10) (2013) 387-395.
- [13] J. Yang, H. Li, T. Wu, W. Zhang, L. Chen, J. Yang, *Adv. Funct. Mater.* 18(19) (2008) 2880-2888.
- [14] F. Aliev, N. Brandt, V. Moshchalkov, V. Kozyrkov, R. Skolozdra, A. Belogorokhov, *Z. Phys. B Con. Mat.* 75(2) (1989) 167-171.
- [15] L. MÜchler, F. Casper, B. Yan, S. Chadov, C. Felser, *Phys. Status Solidi-R* 7(1-2) (2013) 91-100.
- [16] S. Ouardi, G.H. Fecher, B. Balke, X. Kozina, G. Stryganyuk, C. Felser, S. Lowitzer, D. Ködderitzsch, H. Ebert, E. Ikenaga, *Phys. Rev. B* 82(8) (2010) 085108.
- [17] T.M. Tritt, Thermal conductivity: theory, properties, and applications, Springer Science & Business Media 2005.

- [18] S. Bhattacharya, T.M. Tritt, Y. Xia, V. Ponnambalam, S. Poon, N. Thadhani, *Appl. Phys. Lett.* 81(1) (2002) 43-45.
- [19] H. Muta, T. Kanemitsu, K. Kurosaki, S. Yamanaka, *Mater. Trans.* 47(6) (2006) 1453-1457.
- [20] H. Xie, H. Wang, Y. Pei, C. Fu, X. Liu, G.J. Snyder, X. Zhao, T. Zhu, *Adv. Funct. Mater.* 23(41) (2013) 5123-5130.
- [21] A. Matthiessen, M. von Bose, *Phil. Trans. R. Soc. Lond.* 152 (1862) 1-27.
- [22] E.S. Toberer, A. Zevalkink, G.J. Snyder, *J. Mater. Chem.* 21(40) (2011) 15843-15852.
- [23] Y. Pei, H. Wang, G. Snyder, *Adv. Mater.* 24(46) (2012) 6125-6135.
- [24] M. Zebarjadi, K. Esfarjani, M. Dresselhaus, Z. Ren, G. Chen, *Energy Environ. Sci.* 5(1) (2012) 5147-5162.
- [25] T.M. Tritt, *Science* 272(5266) (1996) 1276.
- [26] N.F. Mott, H. Jones, *The theory of the properties of metals and alloys*, Courier Corporation 1958.
- [27] P. Hermet, R.-M. Ayrat, E. Theron, P.G. Yot, F. Salles, M. Tillard, P. Jund, *J. Phys. Chem. C* 118(39) (2014) 22405-22411.
- [28] G.J. Snyder, E.S. Toberer, *Nat. Mater.* 7(2) (2008) 105-114.
- [29] S.R. Culp, S.J. Poon, N. Hickman, T.M. Tritt, J. Blumm, *Appl. Phys. Lett.* 88(4) (2006) 042106.
- [30] J.R. Sootsman, D.Y. Chung, M.G. Kanatzidis, *Angew. Chem. Int. Ed.* 48(46) (2009) 8616-8639.
- [31] G. Mahan, J. Sofo, *Proc. Natl. Acad. Sci.* 93(15) (1996) 7436-7439.
- [32] J.P. Heremans, V. Jovovic, E.S. Toberer, A. Saramat, K. Kurosaki, A. Charoenphakdee, S. Yamanaka, G.J. Snyder, *Science* 321(5888) (2008) 554-557.
- [33] C. Leyens, M. Peters, *Titanium and titanium alloys: fundamentals and applications*, John Wiley & Sons 2003.
- [34] K. Kurosaki, T. Maekawa, H. Muta, S. Yamanaka, *J. Alloys Compd.* 397(1) (2005) 296-299.
- [35] S. Sakurada, N. Shutoh, *Appl. Phys. Lett.* 86(8) (2005) 082105.
- [36] N. Shutoh, S. Sakurada, *J. Alloys Compd.* 389(1) (2005) 204-208.
- [37] T. Sekimoto, K. Kurosaki, H. Muta, S. Yamanaka, *J. Alloys Compd.* 394(1) (2005) 122-125.
- [38] Y.W. Chai, Y. Kimura, *Acta Mater.* 61(18) (2013) 6684-6697.

- [39] Y.W. Chai, Y. Kimura, *Appl. Phys. Lett.* 100(3) (2012) 033114.
- [40] H.J. Hunger, L. Küchler, *Phys. Stat. Sol. (a)* 56(1) (1979).
- [41] G. Gottstein, *Physikalische Grundlagen der Materialkunde*, Springer-Verlag 2007.
- [42] E.J. Mittemeijer, *Fundamentals of Materials Science* (2011) 371-461.
- [43] S.V. Faleev, F. Léonard, *Phys. Rev. B* 77(21) (2008) 214304.
- [44] H. Goldsmid, J. Sharp, *J. Electron. Mater.* 28(7) (1999) 869-872.
- [45] K. Gałazka, S. Populoh, W. Xie, S. Yoon, G. Saucke, J. Hulliger, A. Weidenkaff, *J. Appl. Phys.* 115(18) (2014) 183704.

## List of publications

1. J. Feng *et al.*, “The density and the character of dislocations in spinodal half-Heusler thermoelectrics,” *to be published*.
2. J. Feng *et al.*, “A new approach to enhance half-Heusler thermoelectrics,” *to be published*.

## **Erklärung über die Eigenständigkeit der Diplomarbeit**

Ich versichere, dass ich die vorliegende Arbeit mit dem Titel *Microstructural Evolution in Spinodal Half-Heusler Thermoelectrics* selbständig verfasst und keine anderen als die angegebenen Quellen und Hilfsmittel benutzt habe; aus fremden Quellen entnommene Passagen und Gedanken sind als solche kenntlich gemacht.

## **Declaration of Authorship**

I hereby certify that the thesis entitled *Microstructural Evolution in Spinodal Half-Heusler Thermoelectrics* is entirely my own work except where otherwise indicated. Passages and ideas from other sources have been clearly indicated.

## **Danksagung**

Die vorliegende Arbeit wurde am Max-Planck-Institut für Intelligente Systeme (ehemals Max-Planck-Institut für Metallforschung), Stuttgart, und dem Institut für Materialwissenschaft der Universität Stuttgart durchgeführt. An dieser Stelle möchte ich mich bei allen Personen bedanken, die zum Gelingen dieser Arbeit beigetragen haben.